

TOOLS AND RESOURCES

Experimental toolbox for quantitative evaluation of clathrin-mediated endocytosis in the plant model *Arabidopsis*

Alexander Johnson¹, Nataliia Gnyliukh¹, Walter A. Kaufmann¹, Madhumitha Narasimhan¹, Grégory Vert², Sebastian Y. Bednarek³ and Jiří Friml^{1,*}

ABSTRACT

Clathrin-mediated endocytosis (CME) is a crucial cellular process implicated in many aspects of plant growth, development, intra- and intercellular signaling, nutrient uptake and pathogen defense. Despite these significant roles, little is known about the precise molecular details of how CME functions *in planta*. To facilitate the direct quantitative study of plant CME, we review current routinely used methods and present refined, standardized quantitative imaging protocols that allow the detailed characterization of CME at multiple scales in plant tissues. These protocols include: (1) an efficient electron microscopy protocol for the imaging of *Arabidopsis* CME vesicles *in situ*, thus providing a method for the detailed characterization of the ultrastructure of clathrin-coated vesicles; (2) a detailed protocol and analysis for quantitative live-cell fluorescence microscopy to precisely examine the temporal interplay of endocytosis components during single CME events; (3) a semi-automated analysis to allow the quantitative characterization of global internalization of cargos in whole plant tissues; and (4) an overview and validation of useful genetic and pharmacological tools to interrogate the molecular mechanisms and function of CME in intact plant samples.

This article has an associated First Person interview with the first author of the paper.

KEY WORDS: Quantitative imaging, Clathrin-mediated endocytosis, Metal-replica electron microscopy, Total internal reflection fluorescence microscopy, Confocal microscopy, *Arabidopsis*

INTRODUCTION

Clathrin-mediated endocytosis (CME) is a major mechanism by which plasma membrane (PM) and extracellular cargo, including cell surface receptors and extracellular materials, are internalized into cells (Bitsikas et al., 2014; McMahon and Boucrot, 2011). It is a dynamic and highly regulated multistep process requiring the vesicle coat protein clathrin and a large number of distinct endocytosis accessory proteins (EAPs) recruited to each unique step of the CME process (Kaksonen and Roux, 2018). CME plays an important role in many physiological processes in plants, ranging from growth and


development, cell polarity, intra- and intercellular signaling, nutrient uptake, stress response and pathogen defense (Barberon et al., 2011; Dhonukshe et al., 2007; di Rubbo et al., 2013; Kitakura et al., 2011; Martins et al., 2015; Mbengue et al., 2016; Ortiz-Morea et al., 2016; Yoshinari et al., 2016; Zwiewka et al., 2015). Despite its physiological significance, little is known about the molecular mechanisms of how CME functions in plants, especially compared to mammalian and yeast model systems (Kaksonen and Roux, 2018; Lu et al., 2016).

The great advances in CME studies in mammalian and yeast fields over the past 40 years are mainly thanks to key imaging technologies that have emerged as standard approaches allowing the direct quantitative characterization of CME at very high spatial and temporal resolutions (Kaksonen and Roux, 2018; Lu et al., 2016; Picco and Kaksonen, 2018; Robinson, 2015; Schmid, 2019; Sochacki and Taraska, 2019). For example, electron microscopy (EM) approaches have enabled direct visualization of the clathrin coat itself (Fotin et al., 2004; Heuser, 1980), and live imaging of single CME events on the cell surface have unraveled the complex temporal network of EAPs in live cells (Taylor et al., 2011). Despite the plant field lagging behind in characterization of this key process, in recent years there has been significant progress in identification of evolutionarily conserved and plant-specific EAPs (and in understanding their regulation), which have evolved to meet the unique requirements necessary for plant morphogenesis and growth (Adamowski et al., 2018; Barberon et al., 2011; Bashline et al., 2013; Beck et al., 2012; Dhonukshe et al., 2007; Fan et al., 2013; Gadeyne et al., 2014; Gifford et al., 2005; Kim et al., 2013; Konopka et al., 2008; Martins et al., 2015; Mazur et al., 2020; Paciorek et al., 2005; Sharfman et al., 2011; Takano et al., 2005; Yoshinari et al., 2016; Zhou et al., 2018). Although many of these studies have been driven by the application and optimization of imaging protocols for endocytosis, there is a need for standardization and for approaches that can directly examine plant CME and allow direct comparison of data from different groups, thus improving our ability to work together to characterize this fundamental physiological process.

A major approach to the characterization and identification of bona fide plant EAPs, helping unravel the mechanisms of plant CME, has been the use of biochemical methods such as pull-down assays coupled with mass spectrometry and *in vitro* binding studies. For example, using clathrin light chain 1 (CLC1) as bait, the potential uncoating factor auxilin-like protein was identified (Adamowski et al., 2018). Also, the identification of two major plant EAP complexes (AP2 and TPLATE complexes) were facilitated using similar approaches (di Rubbo et al., 2013; Gadeyne et al., 2014; Yamaoka et al., 2013). Although these methods serve as a good starting point for plant CME characterization, their drawback is that they offer limited insight into the dynamics of the interactions, which are crucial for characterizing a dynamic multistep process such as CME, where each step requires a different subset of EAPs (Merrifield and Kaksonen, 2014). Furthermore, pull-down and *in vitro* binding

¹Institute of Science and Technology Austria, 3400 Klosterneuburg, Austria. ²Plant Science Research Laboratory (LRSV), UMR5546 CNRS/Université Toulouse 3, 24 chemin de Borde Rouge, 31320 Auzeville Tolosane, France. ³UW-Madison, Biochemistry, 215C HF DeLuca Laboratories, Madison, WI 53706, USA.

*Author for correspondence (jiri.friml@ist.ac.at)

 A.J., 0000-0002-2739-8843; N.G., 0000-0002-2198-0509; M.N., 0000-0002-8600-0671; G.V., 0000-0002-0844-9991; S.Y.B., 0000-0001-7465-1787; J.F., 0000-0002-8302-7596

Handling Editor: David Stephens
Received 28 April 2020; Accepted 22 June 2020

studies might not be sufficient to detect many of the key functional CME interactions, as many are reported to be transient (Smith et al., 2017). Therefore, to characterize plant CME precisely, it is crucial that protocols allow direct observation and quantitative assessment of CME *in vivo*. Indeed, the optimization and application of imaging and quantitative analysis protocols in order to visualize CME structures and dynamics *in vivo* has been important for recent advances in our understanding of the molecular mechanisms of plant CME (Fujimoto et al., 2010; Gadeyne et al., 2014; Ito et al., 2012; Johnson and Vert, 2017; Konopka and Bednarek, 2008; Narasimhan et al., 2020; Stefano et al., 2018; Tinevez et al., 2017; Vizcay-Barrena et al., 2011; Wan et al., 2011; Wang et al., 2015; Yamaoka et al., 2013; Yoshinari et al., 2016).

To enhance and facilitate further detailed characterization of plant CME, we briefly review currently available approaches and analytical tools for characterization of the process of CME in plant cells. We also present detailed state-of-the-art microscopy-based methods and guidelines for the quantitative, direct and dynamic examination of CME at multiple scales and for pharmacological and genetic manipulation of CME in intact *Arabidopsis* seedlings.

RESULTS

Methodologies for the imaging and analysis of plant CME

Although there are many different imaging modalities for the study of CME, there are two major categories: electron microscopy (EM) and light microscopy. Each modality offers different strengths and weaknesses based on how they physically function (Fig. 1), which allows investigation of different aspects of CME (Table S1).

EM permits the imaging of subcellular structures, organelles and macromolecular complexes with high spatial resolution, as spatial resolution up to ~4 nm can readily be achieved (de Jonge et al., 2009). These high spatial resolutions are possible because electrons are defined by their higher energy state than photons, which are limited by optical diffraction to resolutions of ~200 nm. Although there are many EM methods, the two classical EM approaches in life sciences are transmission electron microscopy (TEM) and scanning electron microscopy (SEM). They differ in that, in TEM, imaging electrons are detected once they have passed through the sample, whereas SEM detects electrons that are scattered off the sample. As both these methods subject the sample to high-energy electron

stimulation under high vacuum conditions, they are not generally suitable for hydrated organic material with limited electron-dense contrast. The sample must be fixed, dehydrated and contrasted using heavy metals, and then either embedded into a resin for ultrathin sectioning in conventional TEM analysis or replicated in SEM analysis. Thus, there is limited temporal information provided from a sample and one must be careful about the possibility of artifacts produced during sample preparation (Table S1).

There are two main types of light microscopy modalities routinely used to study CME, total internal reflection fluorescence microscopy (TIRF-M) and confocal microscopy. Both offer the possibility of conducting real time imaging of biological samples. The crucial difference is in how they illuminate the sample. TIRF-M makes use of a weak evanescent light wave, generated when the illumination beam hits an interface between two media with different refractive indexes at the critical angle, to illuminate just a small volume of the sample (~100 nm in the Z dimension) (Fig. 1) (Axelrod, 2001; Mattheyses et al., 2010). Confocal microscopy uses a ‘pinhole’ in the optical pathway to physically exclude light from out-of-focus sample planes, allowing researchers to optically section a sample or focus on a single Z plane of interest (Fig. 1). Typically, confocal microscopy refers to confocal laser scanning microscopy (CLSM), which is where a single point scans multiple ‘lines’ across the sample to acquire the whole image. This results in CLSM having a relatively slow acquisition time, which can be overcome using a spinning disk (SD) confocal system. Instead of using a single confocal point to scan the imaging area, a series of pinholes and microlenses are spun in the optical pathway, resulting in multiple confocal ‘points’ in the imaging area (Fig. 1), significantly increasing the speed of acquisition.

Electron microscopy methods; characterization of CME at the ultrastructural level

When EM approaches are combined with protocols for the enrichment of CCVs from plant tissues, as described in detail by Mosesso et al. (2018) and Reynolds et al. (2014), one can begin to define the molecular anatomy of the plant CCV. The disadvantage of examining CCVs isolated from plant tissues is that the preparation could be a mixture of PM- and trans-Golgi network (TGN)-derived CCV populations. Therefore, being able to examine CCVs *in situ* allows direct examination of CCV formations during CME.

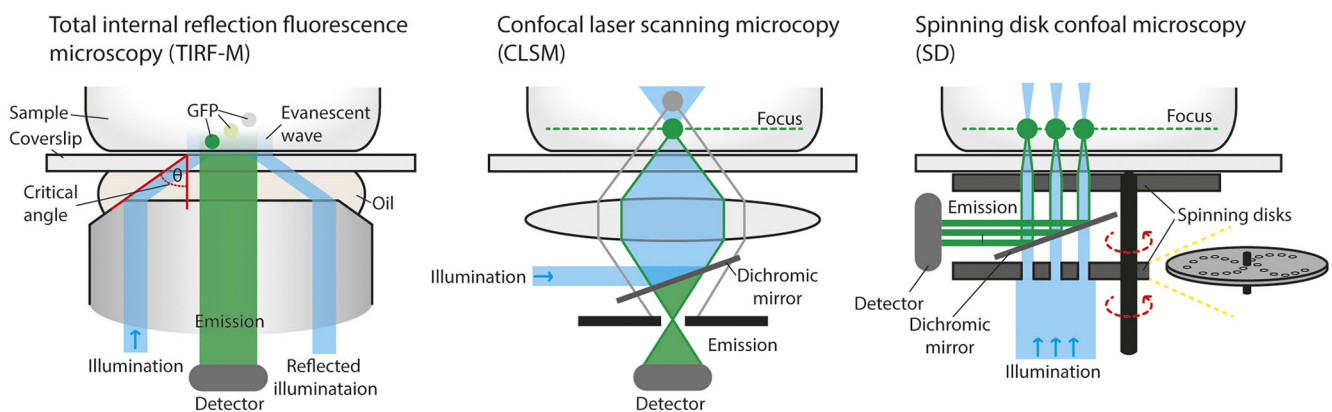


Fig. 1. Principles of the major CME light microscopy methods. TIRF-M uses a weak uniform evanescent wave that penetrates ~100-200 nm into the sample, thereby illuminating cell surfaces in contact with the coverslip. The evanescent illumination wave is generated when the illumination beam hits a refractive index mismatch between the coverslip and sample/medium at the critical angle (θ). The energy of the evanescent wave is directly proportional to the distance away from the point of generation, meaning that fluorophores closer to the PM are stimulated more than those deeper in the cell (green-gray GFP spots). CLSM makes use of a single pinhole, which blocks out-of-focus emitted light from reaching the detector (gray lines). In CLSM, the illumination beam passes directly into the sample. SD confocal microscopy makes use of disks with many pinholes and microlenses that spin rapidly, thus creating many simultaneous confocal points.

Transmission electron microscopy

Transmission electron microscopy (TEM) imaging approaches are widely used in CME studies in other model systems (Sochacki and Taraska, 2019). Whole cells or tissues are fixed and embedded into a resin for ultrathin slicing (40–70 nm). These sections can then be imaged as a single plane through the sample, or serial sections can be aligned and composed to produce a 3D ultrastructural view of the cell. Although TEM has been used routinely in plants, and CCVs are visible and detectable (Bonnett and Newcomb, 1966; Dejonghe et al., 2016; Dhonukshe et al., 2007; Lam et al., 2001; Li et al., 2012; Safavian and Goring, 2013), the preservation of CCVs is incredibly low regardless of the fixing or embedding method used. This has made it extremely difficult to visualize enough CME events to provide a robust quantitative analysis of plant CCVs.

Unroofing metal replica

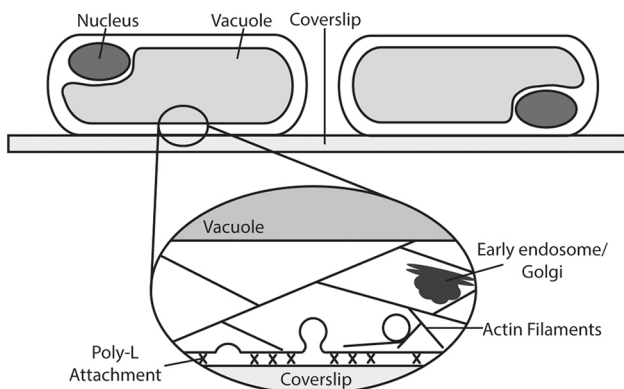
An alternative EM approach for the analysis of CME events is utilization of SEM on ‘unroofed’ plant cells, which enables the PM and its associated CCVs to be visualized. Recently, this approach has been successfully optimized for *Arabidopsis* protoplasts from a suspension of cultured root cells (Narasimhan et al., 2020) and is presented in detail later (‘Expanded method 1’). In this method,

cells are fixed to adherent coverslips and the membranes not in direct contact with the coverslip are ripped away, thereby exposing intact intracellular structures attached to the PM, similar to CCVs undergoing CME (Fig. 2). Therefore, this technique permits the specific examination of budding CME CCVs, as they can be identified by their presence on the PM.

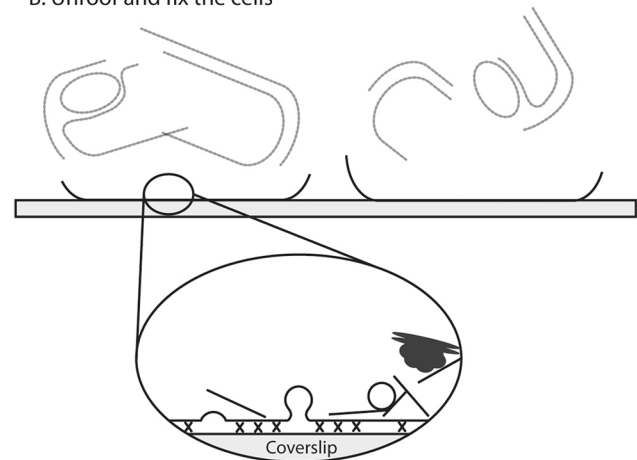
This approach produces images with unprecedented numbers of CCVs in a plant cell *in situ*, compared to previous plant EM approaches, and allows direct characterization of ultrastructural details such as shape, size and stage of CCV formation (Fig. S1). Therefore, this method is suitable for testing the effects of chemical and genetic manipulation on the clathrin coat and on the molecular structure during formation of CME vesicles.

The drawback of this approach is that, at present, it requires the generation of protoplasts. Therefore, one should take into account that the CME-derived CCVs in these cells are formed under physiological conditions that differ from those in cells surrounded by cell walls. Further to this, digestion of the cell wall has been shown to result in intracellular aggregation of certain EAPs (Kang et al., 2003). However, the average CCV size closely matches that of biochemically purified CCVs from plant tissues (Mosesso et al., 2018; Reynolds et al., 2014), suggesting that CCVs in both contexts

A. Attach the cells to the coverslip



B. Unroof and fix the cells



C. Coat the sample with metal

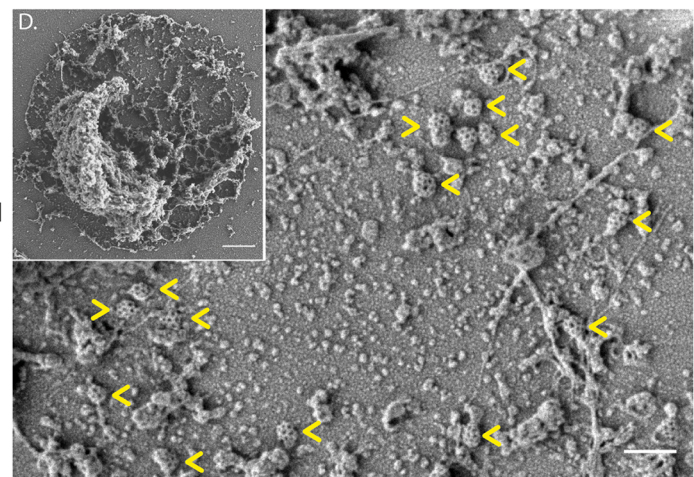
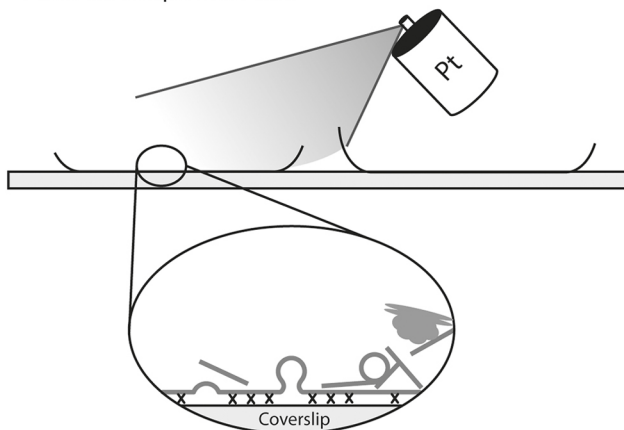


Fig. 2. Unroofing protoplasts and SEM. (A) *Arabidopsis* protoplasts cells are plated onto coverslips coated with poly-L-lysine. (B) The cells are washed with detergent to ‘unroof’ the cells. (C) Unroofed cells are then covered with a thin coat of platinum. (D) Samples are imaged using SEM. The main image shows a high magnification view of a replica in which CCVs associated with the PM are identifiable (yellow arrows). Inset shows a low magnification view of a whole cell replica. Scale bars: 200 nm, 2 μm (inset).

are formed in a similar fashion. A further limitation is accessibility to only the top view of the CCV, which means that hallmark features of the CME, such as the highly curved neck of CCVs, are obstructed by the vesicle itself. Additionally, as the samples are fixed, there is limited temporal information about the CCVs examined.

Methods for directly imaging the PM; characterization of CME at the single event level

The PM is a major site of CME, therefore high-resolution imaging of just the PM allows direct visualization of single CME events (Fig. 3). We can define the precise temporal characteristics of plant CME (Figs 3,4,5) by combining the imaging of single events, which can be marked using established EAP plant lines (Table S2), with high-throughput analysis protocols (see ‘Expanded method 2’).

The methods presented in ‘Expanded method 2’ use an unbiased automated high-throughput analysis system for quantitative analysis of cell surface imaging data. Specifically, we made use of the detection and tracking components of the *cmeAnalysis* package (Aguet et al., 2013) and further processed the data with our own scripts (see ‘Expanded method 2’, note 7). This is because the processing step in the *cmeAnalysis* package, which is used to define bona fide CME events, is optimized for mammalian systems and fails to identify bona fide plant CME events accurately (Johnson and Vert, 2017). This approach provides several significant advantages over manual methods for detection and quantification of time-lapse image sequences of CME events in plant cells. For example, the analysis is based on the parameters of the experimental setup and each detection is statistically tested, removing subjective human input/bias (Aguet et al., 2013). Furthermore, the number of events analyzed by the described automated workflows is far larger than

can be readily achieved by manual tracking, thus giving greater statistical significance and reproducibility of results.

Single-channel EAP cell surface analysis

Live-cell imaging of the PM in samples expressing EAPs tagged with fluorescent protein, combined with automated unbiased detection, tracking and analysis provides key quantifiable physiological metrics to enable analysis of the dynamics of plant CME. For example, live TIRF-M of clathrin light chain 2 (CLC2) and quantification using our automated single-channel analysis (Fig. 4A-F) (see ‘Expanded method 2’) gives the lifetimes (Fig. 4G,H), density (Fig. 4I) and fluorescent intensity profiles (Fig. 4F,J) of CLC2-labeled clathrin-coated pits. The lifetimes of clathrin and other EAPs on the cell surface can provide information about the overall kinetics of CME. The density of EAPs is informative about the overall amount of CME occurring in a region of interest within the cell. The mean fluorescent profile of cell surface EAPs can provide clues regarding their functions: as CME is a reaction where CLC polymerizes on a budding vesicle on the PM until freed from the PM, one can expect its fluorescence profile to reflect this process (Fig. 3B,C; Fig. 4F,J).

A major issue with single-channel cell surface imaging data is that the total population of the chosen marker protein is measured on, or near, the cell surface. Therefore, the results include information about additional cellular processes that affect the lifetime and density of proteins at the PM, including its *de novo* synthesis, trafficking and recycling/degradation. If single-channel images are used to assess the kinetics of CME, the results should be validated by population modeling (Loerke et al., 2009) and/or by dual-channel imaging of bona fide CME marker proteins together

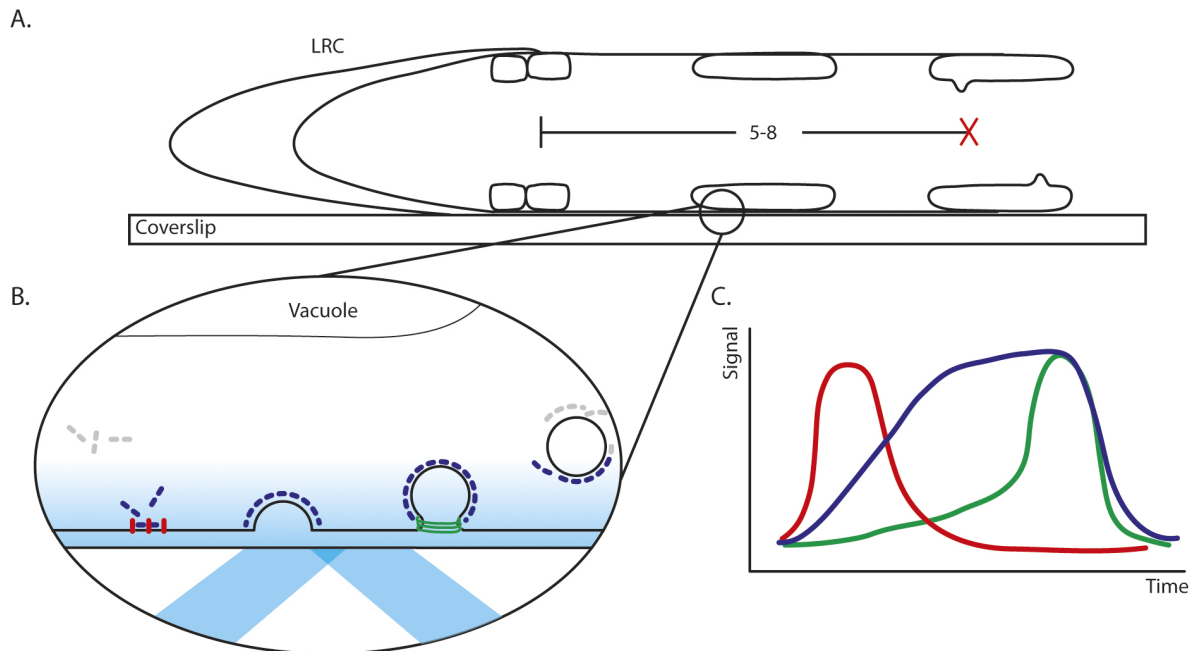


Fig. 3. Cell surface TIRF-M imaging. (A) To facilitate TIRF-M, the sample needs to be flat and in direct contact with the coverslip. The location of imaging within the root is crucial to obtaining reproducible results. The end of the lateral root cap (LRC) is used as a developmental marker, and cells 5-8 up the root are used for imaging. (B) Lifetimes of proteins on the PM are only measured when the protein is within the illumination volume. (C) Time and intensity fluorescent profiles of proteins can provide hints about their physiological function. For example, as clathrin triskelions containing fluorescently labeled clathrin subunits (blue) polymerize on the PM to form invaginating clathrin-coated pits, there is an increase in the level of fluorescence signal. Upon scission of the labeled CCVs from the PM, they rapidly depart from the illumination field resulting in a sharp decrease in fluorescence signal. Dual-channel imaging of proteins of interest with a fluorescently tagged clathrin marker permits quantitative comparison of its temporal dynamics relative to the clathrin-coated pit initiation, maturation and CCV departure from the PM (green and red examples as depicted in B).

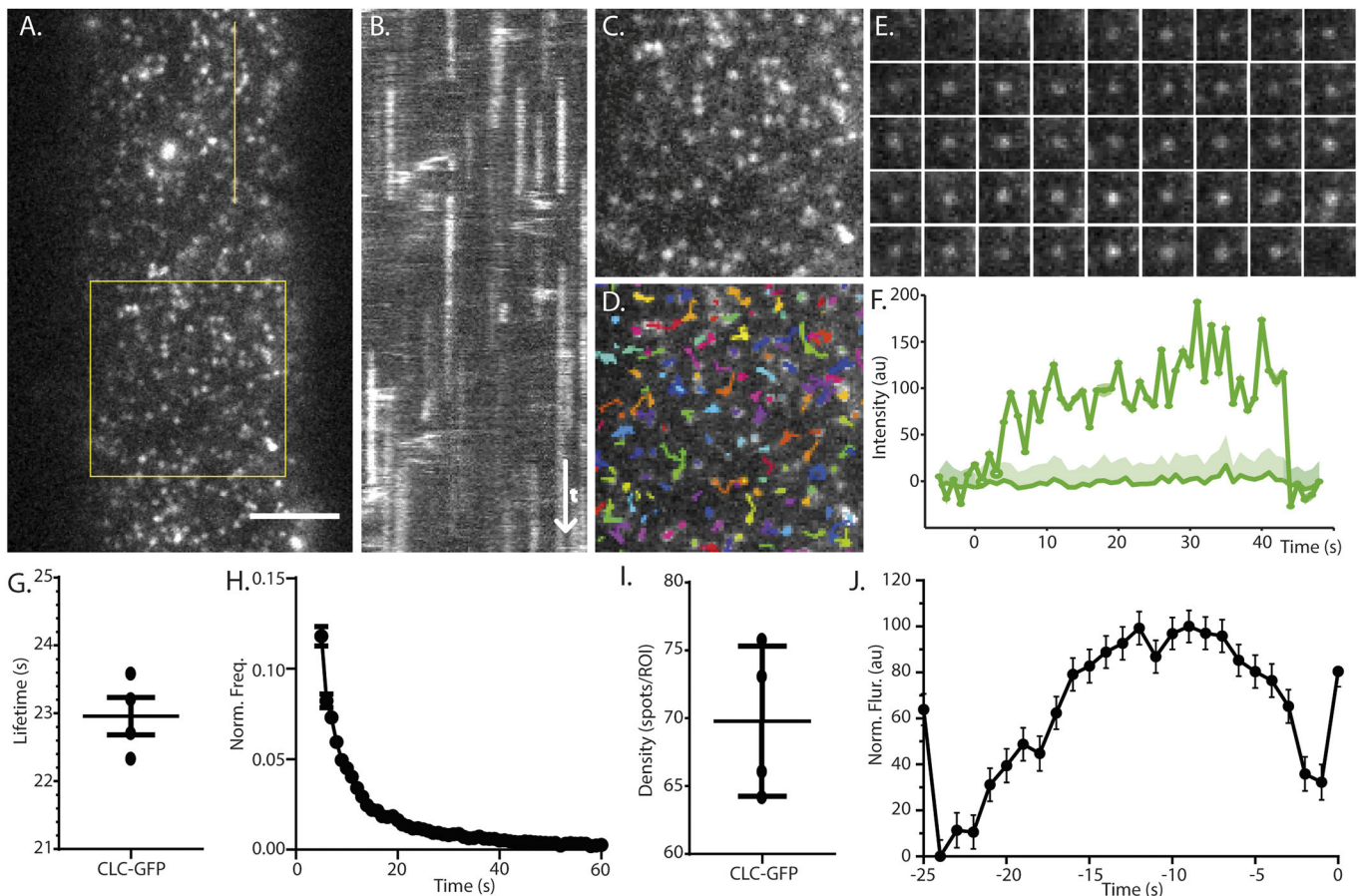


Fig. 4. Single-channel TIRF-M cell surface analyses. (A) Example TIRF-M image from a root epidermal cell expressing CLC2-GFP. (B) Example kymograph generated for the yellow line in A. (C) Magnified image of the region of the yellow square in A. (D) Results of the automated detection and tracking analysis. (E) Time series of an example single CLC event on the PM. (F) Quantification of the lifetime of the event based on the fluorescent intensity profile, which is significantly above the intensity of surrounding pixels. (G–J) Tracking data from multiple independent tracks and experiments are combined to generate a mean lifetime (G), lifetime distribution (H), mean density of spots (I) and mean fluorescent profile (J). Plots indicate mean \pm s.e.m. $n=4$ cells from independent roots, 20,098 tracks. Scale bar: 5 μ m.

with the protein of interest (Narasimhan et al., 2020). Once it has been established that a protein of interest functions in CME, single-channel cell surface imaging can be utilized to test the effect of pharmacological and genetic manipulation on its recruitment and kinetics in CME (Tables S3 and S4).

Dual-channel EAP cell surface analysis

To overcome the limitations of single-channel cell surface imaging, dual-channel imaging can be conducted with a second marker for CME. For example, examining the dynamics of an EAP that colocalizes with a second marker for CME, such as clathrin, aids the filtering of CME events to consider only bona fide events. Our analysis provides the same output metrics as single-channel analysis (lifetime, density and fluorescent intensity profile), but only for events where both markers are detected.

The greatest advantage of using dual-channel cell surface imaging for the analysis of CME is that a departure assay can be conducted. This automated unbiased analysis allows precise determination of when an EAP is recruited to CME events, relative to a well-characterized marker of CME such as CLC2 (Johnson and Vert, 2017; Konopka et al., 2008; Mattheyses et al., 2011; Merrifield et al., 2002). In the departure assay, the fluorescence intensity profile of the candidate EAPs (in the secondary channel) is aligned to the end of the profile for CLC2 (in the primary channel) as this represents the

moment a CME vesicle is scissioned from the PM and is able to leave the field of illumination (Fig. 3B,C; Fig. 5). This gives a physiological reference on which to base the temporal dynamics of EAPs at single events of CME. This analysis of EAP dynamics therefore requires that the EAP of interest is coexpressed with a bona fide CME marker whose dynamics have been well characterized.

Comparison of cell surface imaging techniques for CME visualization on the PM

As the lifetimes of plant bona fide CME events are quite rapid (42 s in root cells and 33 s in hypocotyl) (Narasimhan et al., 2020), it is necessary that imaging is conducted using either TIRF-M or spinning disk (SD) confocal microscopy, which provide sufficient spatial and temporal resolution to capture CME events on the PM. However, TIRF-M provides a higher signal-to-noise ratio and sensitivity than SD confocal imaging and is thus better suited for detecting the early stages of CME, as many of the ‘early stage’ EAPs are present in low numbers (Mettlen and Danuser, 2014). An additional benefit of the higher sensitivity of TIRF-M is that less laser power is required for excitation, thus reducing phototoxicity effects and increasing the duration over which it is possible to acquire images. This is because TIRF-M limits the illumination volume of the sample and uses a low intensity evanescent wave, where all the emitted photons are collected. In contrast, SD

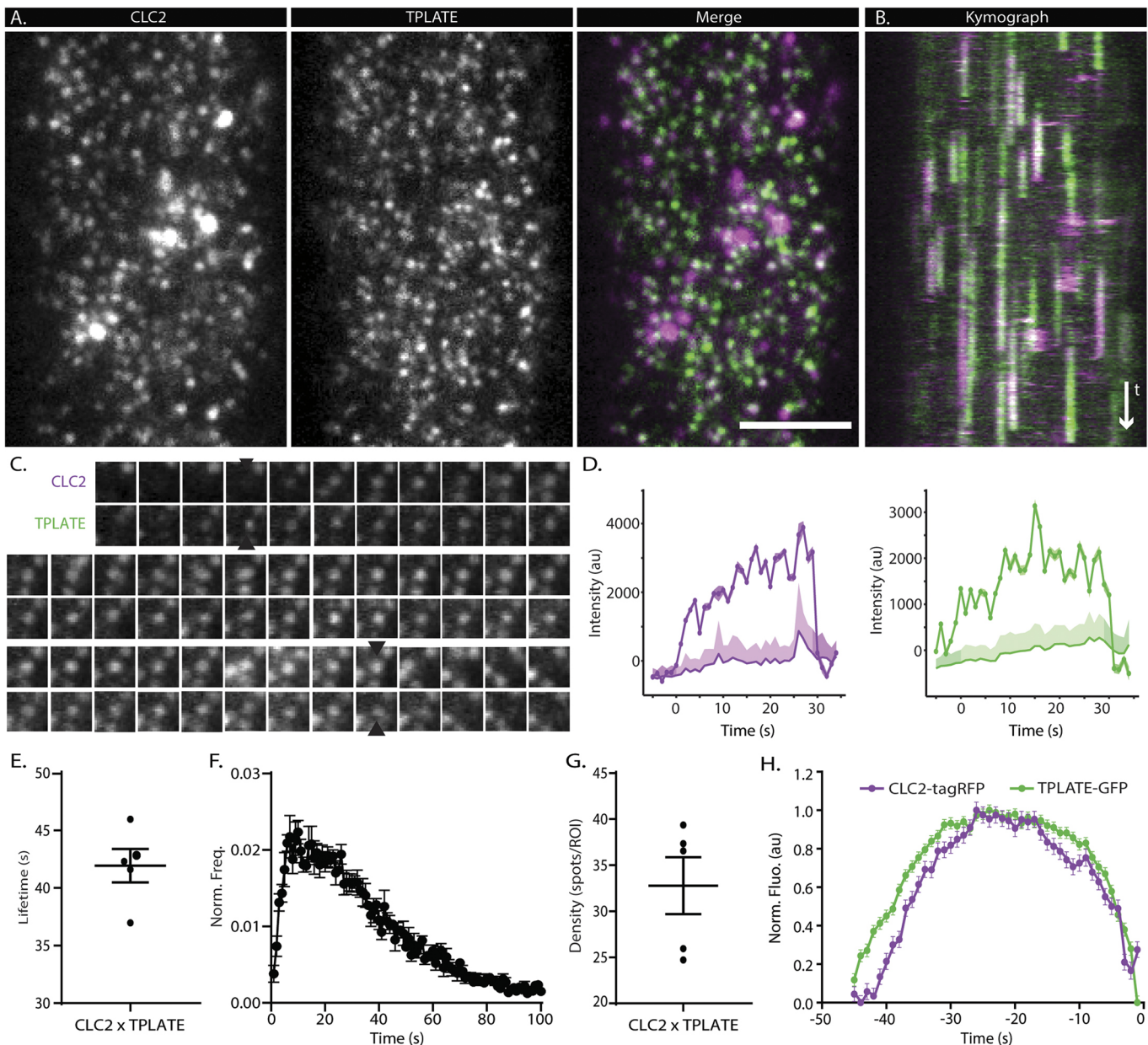


Fig. 5. Dual-channel TIRF-M cell surface analyses. (A) TIRF-M images of a root epidermal cell expressing fluorescently tagged CLC2-tagRFP and TPLATE-GFP. (B) Representative kymograph of CLC and TPLATE lifetimes on the PM. (C) Example of time-lapse image sequence from the single endocytic event positive for both CLC2 and TPLATE. Black arrows mark the appearance and disappearance of the fluorescence signals on the PM. Each frame represents 1 s. (D) Fluorescence intensity quantification of the CLC2 (magenta) and TPLATE (green) spots in the example image sequence of the single CME event shown in C. (E-H) Data from five independent experiments were combined to generate a mean lifetime (E), lifetime distribution (F), mean density of CME events (G) and mean recruitment profile of TPLATE to the site of endocytosis (H). Plots indicate mean \pm s.e.m. $n=5$ cells from independent roots, 11,361 tracks. Scale bar: 5 μ m.

microscopy uses pinholes to block out-of-focus photons, and the whole sample is illuminated (Fig. 1). The major disadvantage of TIRF-M is that the shallow illumination volume means that it can only be applied to imaging of cell surfaces that are in direct contact with the coverslip. For this reason, TIRF-M has been used almost exclusively to image epidermal cells of seedling roots and hypocotyls, whereas SD confocal microscopy gives greater flexibility in terms of which tissues and cell surfaces can be imaged.

As an alternative to TIRF-M and SD confocal microscopy, variable-angle epifluorescence microscopy (VAEM) (Chen et al., 2018; Higaki, 2015; Konopka and Bednarek, 2008; Wan et al., 2011), also known as highly inclined thin illumination (HILO)

microscopy (Tokunaga et al., 2008), can be used. It overcomes some of the limitations of confocal systems (their lack of sensitivity for low levels of signal intensities) and TIRF-M (the shallow illumination volume). Instead of using TIRF illumination, the angle of incidence of the excitation beam is oblique such that it undergoes refraction, instead of reflection, towards the coverslip. In images where the excitation beam penetration is relatively shallow, the signal-to-noise ratio of VAEM/HILO approaches that of TIRF-M (Wan et al., 2011). However, the depth of Z penetration is not uniform across the image (Fig. S2B), which can introduce variability when trying to measure the dynamics of proteins in a single Z plane, such as EAPs on the PM.

Considerations for the use of fluorescent protein-tagged reporters

The choice of fluorescent protein tags for imaging CME reporter proteins is an important consideration as they all have different properties (e.g. excitation/emission spectra, brightness and photostability). An excellent resource for further information on the various available genetically encoded fluorescent protein tags and their parameters is the Fluorescent Protein Database (<https://www.fpbase.org>) (Lambert, 2019).

A crucial consideration when analyzing the localization and dynamics of fluorescent tagged proteins of interest is the expression level of that protein, as one must consider that grossly overexpressing proteins involved in CME could affect the dynamics of the process. It is therefore good practice to use fluorescent fusion proteins that have been demonstrated to be functional (e.g. through their ability to rescue the phenotype of corresponding loss-of-function mutant lines) (Table S2) and whose expression level is close to that of the endogenous protein of interest. However, from a practical standpoint, the intensity of the candidate EAP fluorescence signal must be sufficiently above background in order for it to be detected by the instrumentation and detection software.

In recent years, it has been considered best practice for studies of mammalian and yeast CME to utilize gene-edited cells and systems for expression of fluorescent proteins of interest, as the lifetime of certain EAPs is reportedly altered when transiently overexpressed (Doyon et al., 2011). However, it is important to note that the reported temporal difference between transient overexpression versus stable expression of CME reporters in gene-edited cells was subsequently found to be a result of differences in sensitivity of the analysis software used. In particular, the recruitment and/or dynamics of fluorescent fusion protein-tagged CLC2 were not affected by overexpression when analyzed using the robust and sensitive detection system of the *cmeAnalysis* package (Aguet et al., 2013).

Methods for the quantitative analysis of cargo internalization; characterization of CME at the whole tissue level

Examination of the uptake of fluorescently labeled cargo, or dyes, from the PM provides another approach for assessing CME in plants (Table S5). This is because, after the CME event has occurred, cargo is trafficked to the TGN/early endosomes where it is either trafficked to the multivesicular bodies for delivery and degradation in the vacuole and/or recycled back to the PM. Therefore, quantitative analysis of the intracellular levels of fluorescently labeled marker internalized from the PM, after a short time period, provides another approach for assessing the activity of the plant CME machinery and its regulation.

FM dyes

FM dyes are a series of amphiphilic styryl dyes that are used as tools in model systems to measure net internalization of the PM (Bolte et al., 2004; Cheung and Cousin, 2011; Jelínková et al., 2010; Mueller et al., 2004). These dyes contain a central region that is flanked by a hydrophobic tail and a polar head group (Fig. 6A) (Betz et al., 1996). The central region determines the fluorescence properties of the dye; for example two commonly used FM dyes in plant CME studies are FM4-64 and FM1-43, whose peak fluorescent emissions are in the red (Fig. 6B) and yellow (Fig. S3A,B) spectrum, respectively. The hydrophobic tail can reversibly associate with the outer leaflet of membranes, resulting in a dramatic increase in their fluorescence quantum yield relative to

their non-membrane bound state (Henkel et al., 1996). The polar head group prevents the FM dyes from being able to cross the PM, meaning that their entry into cells is solely dependent on endocytosis (Fig. 6C-E).

To assess the level of PM endocytosis, cells are incubated with the FM dye and the level of internalized intracellular fluorescence signal is subsequently measured and compared with the signal of FM dye remaining on the PM. By using confocal-based microscopy, these types of experiments provide the opportunity to analyze endocytosis at the cellular and whole tissue levels. As the only material requirement is the dye, they represent a rapid and convenient experimental approach for testing the effects of pharmacological or genetic manipulation of CME, with no need to generate genetic marker plants lines or crosses. To quantify precisely the total amount of FM dye internalization, 3D imaging and analysis of the entire volume of a cell is required. This type of analysis is feasible for analyzing individual cells (Rosquete et al., 2019). However, a major challenge with the quantification of FM dye endocytosis in plant tissues is the non-uniform geometry of cells within the tissues. When projected in 3D, this results in images with an undefinable PM region, making evaluation of the levels of PM FM dye signal relative to intracellular FM dye signal prone to a subjective bias.

To date, the majority of FM dye uptake studies in plants have relied on the use of manual approaches to segment the PM and intracellular regions within single z-section image planes. Therefore, to facilitate the unbiased quantification of the total amount of FM dye labeling in both the PM and intracellular compartments, we have developed a semi-automated analysis that is based on segmentation of the membrane and intracellular regions to provide a robust method for FM uptake quantification (see 'Expanded method 3'; Fig. 6E-G). Using this analysis, we found that the efficiency of internalization of FM4-64 and FM1-43 are similar (Fig. S3C,D). Due to the nature of the automated segmentation, whole fields of view can be analyzed rapidly and only cells that are in a similar focal plane are segmented, thereby removing manual selection and segmentation bias. Although this analysis tool overcomes many of the previous difficulties in quantification of FM dye uptake, analysis of the internalization of PM cargo in plant tissues and individual cells remains constrained to quantification of the level of FM dye signal within a single Z focal imaging plane.

A major consideration when using FM dyes to measure endocytosis is that their internalization is mediated by both CME and clathrin-independent endocytosis (CIE) internalization pathways. Additionally, it has been reported that FM dye labeling could perturb the localization of certain plant membrane proteins (Jelínková et al., 2010). Nonetheless, despite these concerns, FM dye uptake studies have been and will continue to be an effective and informative tool for assessing global endocytosis in plant tissues.

Fluorescently labeled cargo uptake assays

To examine the CME internalization pathway specifically, one should make use of labeled known cargos of the CME internalization pathway. This requires a bona fide CME cargo protein. Recent studies have led to the identification of a number of plant cell surface proteins that undergo constitutive and/or ligand-dependent CME, including PIN2, BOR1 and BOR4, FLS2, BRI1, IRT1, CEAS, PEPR1 and STRUBBELIG (Barberon et al., 2014; Bashline et al., 2013; Dhonukshe et al., 2007; di Rubbo et al., 2013; Gao et al., 2019; Ortiz-Morea et al., 2016; Takano et al., 2005;

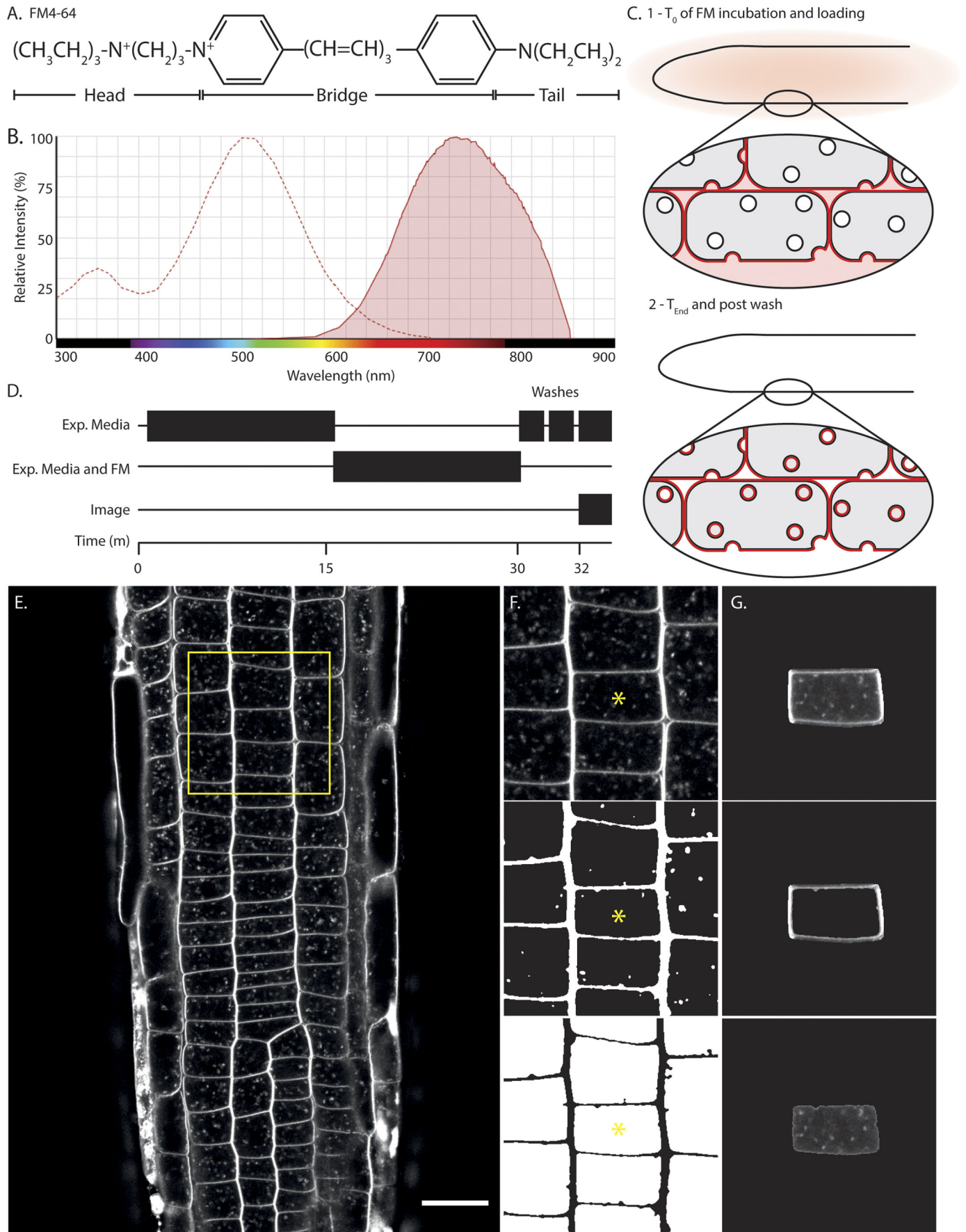


Fig. 6. See next page for legend.

Fig. 6. FM4-64 uptake assay. (A,B) The chemical structure (A) and fluorescence excitation/emission spectra (B) of FM4-64 (adapted from ThermoFisher Bioscience Fluorescence SpectraViewer). (C) Scheme of FM dye uptake assay. At T_0 the plant is incubated with the dye and at T_{end} , after washing the non-internalized dye away, FM dye is internalized via endocytosis from the PM. (D) Basic FM experimental plan. (E) Example CLSM image of the epidermal layer of *Arabidopsis* root after incubation with FM dye. (F) Top: zoom of the region of interest marked by the yellow square. Middle: example of the automated membrane. Bottom: (intracellular) thresholding used for quantification. (G) Example of a single cell and its PM and intracellular segmentations (yellow asterisks in F), which are used to calculate the ratio between the PM and intracellular signals. Scale bar: 20 μm .

Yoshinari et al., 2016). However, the expression of many of these proteins is often restricted to specific cell types, cellular domains and specific physiological conditions; thus, they are not well suited as general markers for the analysis of plant CME (Qi et al., 2018). Further work is needed to identify a ubiquitously expressed and constitutive recycling cargo protein to serve as a general marker for plant CME. A defined cargo satisfying these requirements in plants would provide researchers with a reference tool for direct and specific examination of the CME pathway in plants, in all cells and tissues, without the requirement for activation of the CME reaction.

One attempt to overcome these issues has been the use of the canonical mammalian CME cargo, human transferrin receptor (hTfR). It has been demonstrated that *Arabidopsis* protoplasts are able to transiently express and recycle hTfR (Ortiz-Zapater et al., 2006), thus providing a rapid experimental system in which one can assess the rate of CME under different experimental conditions and treatments (Robert et al., 2010). However, this approach relies on a non-native plant cargo in order to examine the evolutionarily unique process of plant CME. Additionally, researchers have made use of transient expression of CME-related proteins and cargos in tobacco leaf pavement cells as a rapid experimental alternative to generation of novel plant lines (Bandmann et al., 2012; Cao et al., 2020; Gadeyne et al., 2014; Leborgne-Castel et al., 2008; Mbengue et al., 2016). However, it is important to consider that examination of a protein of interest relies on its overexpression, and there appears to be differences in the vesicle trafficking machinery/processing between *Arabidopsis* and tobacco (Langhans et al., 2011).

Photoconvertible fluorescent tags of CME cargos

Photoconvertible fluorescent tags such as EOS or Dendra can provide information about specific populations of tagged proteins. This is because stimulation with a high intensity 405 nm laser burst changes their emission spectra irreversibly from green to red (Gurskaya et al., 2006), thereby enabling discrimination between distinct protein populations that differ in terms of their subcellular distribution. In the case of CME cargo proteins that reside at the PM, the use of photoconversion permits direct examination of the uptake of a specific cargo in any plant tissue and has been utilized in plants to address the internalization of PIN cargos and their regulation by plant hormones (Jásik et al., 2016; Salanenka et al., 2018). As these assays specifically look at a defined cargo, they can provide greater insight into how CME is utilized by the cell in cellular processes. For example, in cases where PIN2-Dendra has been utilized to examine its internalization via CME, this direct approach has shown that the PIN2 dynamics reported from indirect measures of CME were not physiologically accurate (Jásik et al., 2016; Kleine-Vehn et al., 2008b).

Crucially, as one is looking specifically at a certain cargo, the internalization pathway of this cargo should be well defined, for example in terms of clathrin-dependent and -independent internalization.

Probing the mechanisms of CME through pharmacological and genetic manipulation

A classical way to determine the mechanisms underlying a biological process is to disrupt it using pharmacological agents and/or through genetic manipulation. In this manner, testable hypotheses regarding the function of proteins of interest can be formulated and experimentally evaluated. Pharmacological and genetic manipulations that interfere directly with the process of CME (Tables S3 and S4) are very useful tools for the general study of plant endocytic trafficking at multiple scales. Pharmacological agents are advantageous because of their rapid action, application and reversibility upon removal. In contrast, the use of genetic manipulation allows the customized targeting of specific proteins, domains and interactions. Both approaches can be used in conjunction with the expanded methods presented in this paper.

Brefeldin A

An example of an internalization assay for labeled CME cargos combined with pharmacological disruption of the trafficking pathway to study CME is the use of Brefeldin A (BFA). BFA is a fungal metabolite that interferes with interactions of certain ARF GTPases and GEFs (Helms and Rothman, 1992), resulting in the reversible agglomeration of misshaped endosomal and Golgi compartments (Geldner et al., 2001; Grebe et al., 2003), which are often referred to as ‘BFA bodies’. Within these BFA bodies, endocytic cargo and newly synthesized secretory proteins become entrapped and are prevented from entering downstream trafficking pathways to be degraded or recycled. The levels of PM proteins in BFA bodies can thus be used as a proxy to estimate internalized CME cargo. Indeed, it has been shown that many cell surface cargos colocalize with BFA bodies (Beck et al., 2012; Gifford et al., 2005; Karlova et al., 2006; Kwaaitaal et al., 2005); thus, the rate of internalization of PM-associated proteins can be determined by measuring the signal intensity of fluorescent endocytic reporters upon entrapment in BFA bodies. However, to discriminate between the accumulation of endocytic cargo versus newly synthesized proteins in BFA bodies, the sample needs to be treated with both BFA and the protein synthesis inhibitor cycloheximide.

Although BFA treatment often provides a quick and easy estimate of the rate of internalization of different cargos, it is a problematic approach for multiple reasons. The first consideration is that cells of different tissues and developmental stages show different sensitivities to BFA. Another issue is that the ‘BFA body pathway’ is not a common pathway for all potential CME cargos (Russeinova et al., 2004); thus, the cargo used in such experiments must be well characterized. Further concerns are that BFA has been reported to partially inhibit endocytosis at least of some cargos (Naramoto et al., 2010) and that some endocytic cargos (such as PINs) gradually disappear from the BFA bodies after prolonged incubation (Kitakura et al., 2011; Kleine-Vehn et al., 2008a). The most problematic issue is that BFA not only leads to intracellular accumulation of endocytic cargos but also to the aggregation of endosomes, TGN and Golgi at the periphery (Naramoto et al., 2014). Therefore, the cargo accumulation in BFA bodies is a net result of all these processes and so the outcome needs to be interpreted with caution.

Specific CME pharmacological agents

Pharmacological manipulation of EAPs and CME are routinely used in CME investigation, where most of the drugs have been developed in other model systems (Dutta and Donaldson, 2012; von Kleist and Haucke, 2012). Recent advances in our understanding of

plant CME have shown that plant CME functions in many evolutionarily unique ways; thus, when using inhibitors from non-plant systems it is important to validate their activity and examine potential off-target effects. For example, a commonly used CME inhibitor, tyrothostin A23 (TyrA23) (Banbury et al., 2003), was found to operate through distinct mechanisms. In animal cells, TyrA23 targets the EAP AP-2 complex but in plant cells it acts predominantly by disrupting intracellular pH gradients (Dejonghe et al., 2016). Additionally, although the small molecule inhibitor of mammalian CME, Pitstop 2, reduces FM dye uptake in a concentration-dependent manner, internalization of CME cargos was not inhibited in *Arabidopsis* seedlings (Dejonghe et al., 2019).

To circumvent these issues, the novel ES9-17 compound was designed in order to produce a specific block of CME in plant tissues (Dejonghe et al., 2019). It targets clathrin heavy chain (CHC) but without the off-target protonophore effects of its predecessor endosidin 9 (ES9). The impact of ES9-17 on trafficking was analyzed using a variety of assays, including FM4-64, cargo uptake and EAP lifetime on the PM (Table S3). ES9-17 produced a very strong block of FM dye uptake and prolonged the lifetime of EAPs, which suggests that it reliably blocks plant CME (Dejonghe et al., 2019). However, it is important to note that the effects of ES9-17 might not be restricted to CME as CHC is also involved in post-Golgi clathrin-dependent trafficking, rather than just CME at the PM.

In addition to CME inhibitors that target AP2 and clathrin, several compounds that interfere with other essential EAPs have been tested in plant samples. For example, the mammalian dynamin GTPase inhibitors Dynasore and a more potent analogue, Dyngo 4a, have been tested on plant tissues (Hunter et al., 2019; Mcluskey et al., 2013). Here, we demonstrate using TIRF-M that Dyngo 4a also prolongs the lifetime of CLC2 in intact *Arabidopsis* root tissues (Fig. S4). This prolongation, rather than stalling of CLC2 on the PM, suggests that Dyngo 4a might not have such a strong affinity for plant dynamin-related proteins (DRPs) as for mammalian dynamins. It is important to note that because Dyngo 4a absorbs light in the range of about 500–700 nm it is unsuitable for use in studies with FM dyes 4-64 and 1-43 (peak emissions at 725 nm and 580 nm, respectively) (Fig. S5 and unpublished observations from multiple laboratories).

Ikarugamycin (IKA), a naturally occurring compound, has also been used to inhibit CME in plant and mammalian systems (Bandmann et al., 2012; Elkin et al., 2016; Moscatelli et al., 2007). Although its mechanism of action is not known, IKA is reportedly specific for the CME pathway in mammalian systems (Elkin et al., 2016). We therefore tested its effect on plant CME in intact *Arabidopsis* root samples. We showed that treatment of *Arabidopsis* roots with 30 μ M IKA for 15 min did not completely block FM4-64 uptake but did result in a significant increase in persistent cell surface foci of CLC2, suggesting that IKA specifically inhibits CME-mediated FM dye uptake, but not clathrin-independent endocytosis (Fig. 7A,B). However, caution is required until its precise mechanism of function is uncovered.

Genetic manipulations of EAPs to investigate plant CME

Analysis of mutants that disrupt the expression of proteins involved in CME is a powerful approach for validating the function of key plant CME EAPs (Table S6). However, for plant CME, there appears to be an extensive amount of functional redundancy; for example, mutations in the individual genes encoding the two *Arabidopsis* CHC isoforms (CHC1 and CHC2) display no, or only weak, CME defects (Kitakura et al., 2011). Another complication with the genetic analysis of proteins involved in CME in plants is

that mutations that result in the complete loss of expression of essential proteins are homozygous lethal. Likewise, loss-of-function mutants in genes encoding subunits of the TPLATE complex (TPC), a key plant-specific EAP, result in pollen lethality (Gadeyne et al., 2014).

An alternative approach for the analysis of proteins involved in CME that are encoded by essential genes is the use of conditional mutants. This allows modification of the timing of downregulation of expression and facilitates the characterization of their function to stages of plant development and/or tissues more tractable for live-cell imaging and cargo uptake studies. Use of conditional mutants is also advantageous as it limits the possibility for the plant to develop compensatory mechanisms. For example, to overcome the pollen lethality associated with loss-of-function mutation in genes encoding TPLATE and other subunits of the TPC, inducible artificial micro-RNAs (amiR) have been used to silence the expression of TPLATE in seedlings, thereby permitting analysis of the function of the TPC in CME (Gadeyne et al., 2014; Wang et al., 2016). Similar conditional amiR knockdown strategies have been successfully used to study the role of other key plant EAPs (Table S4).

A complementary approach for the analysis of essential and/or functionally redundant proteins involved in CME is to utilize inducible overexpression of wild-type or dominant-negative versions of proteins of interest to regulate the process of CME (Table S4). For example, inducible overexpression of *Arabidopsis* auxilin-like proteins (homologues of the mammalian auxilin protein involved in CCV uncoating) abolished the formation of CME foci at the PM (Adamowski et al., 2018). Overexpression of the C-terminus of CHC1 (termed CHC HUB), which binds and prevents CLCs from forming the CCV, has also been shown to disrupt CME effectively (Dhonukshe et al., 2007). Similarly, overexpression of a dominant-negative GTPase-defective DRP1a resulted in significant extension of the lifetime of CLC2 on the PM (Yoshinari et al., 2016). However, it is important to consider potential off-target effects of the use of dominant-negative constructs in other cellular processes.

Quantitative analysis of CME inhibition

The inhibitory effects of both pharmacological treatment and genetic mutations on CME can be assessed at the ultrastructural and global levels using assays such as the FM4-64 uptake method detailed in 'Expanded method 1' and 'Expanded method 3'. However, to determine the effects at single events on the PM, additional analysis is required as cell surface lifetime analysis alone is not sufficient to quantify reliably the effects of inhibitors and/or genetic manipulation of the dynamics of individual CME events. A major reason for this is that quantification of the lifetime of clathrin and EAPs at the PM involves measuring the duration (i.e. time between the initiation and disappearance) of CME marker proteins recruited to CME events. Inhibition of CME manifests in non-productive CME events (i.e. stalled or delayed) in which clathrin and/or EAP marker proteins are present before and after the image acquisition window, thus preventing or reducing visualization of their appearance and disappearance, making it almost impossible to determine their lifetimes accurately. Therefore, we developed an alternative robust method to quantify the level of inhibition of CME dynamics following pharmacological and/or genetic manipulation, termed the 'spot persistence assay' (Fig. 7C). The procedure measures the duration of EAP foci on the PM to determine a ratio between the number of dynamic and persistent foci of EAPs within the first 100 s of a cell surface imaging experiment (see 'Expanded method 4'). The 100 s window is used because it is over twice the duration of the mean lifetime of bona fide CME events (42 s in

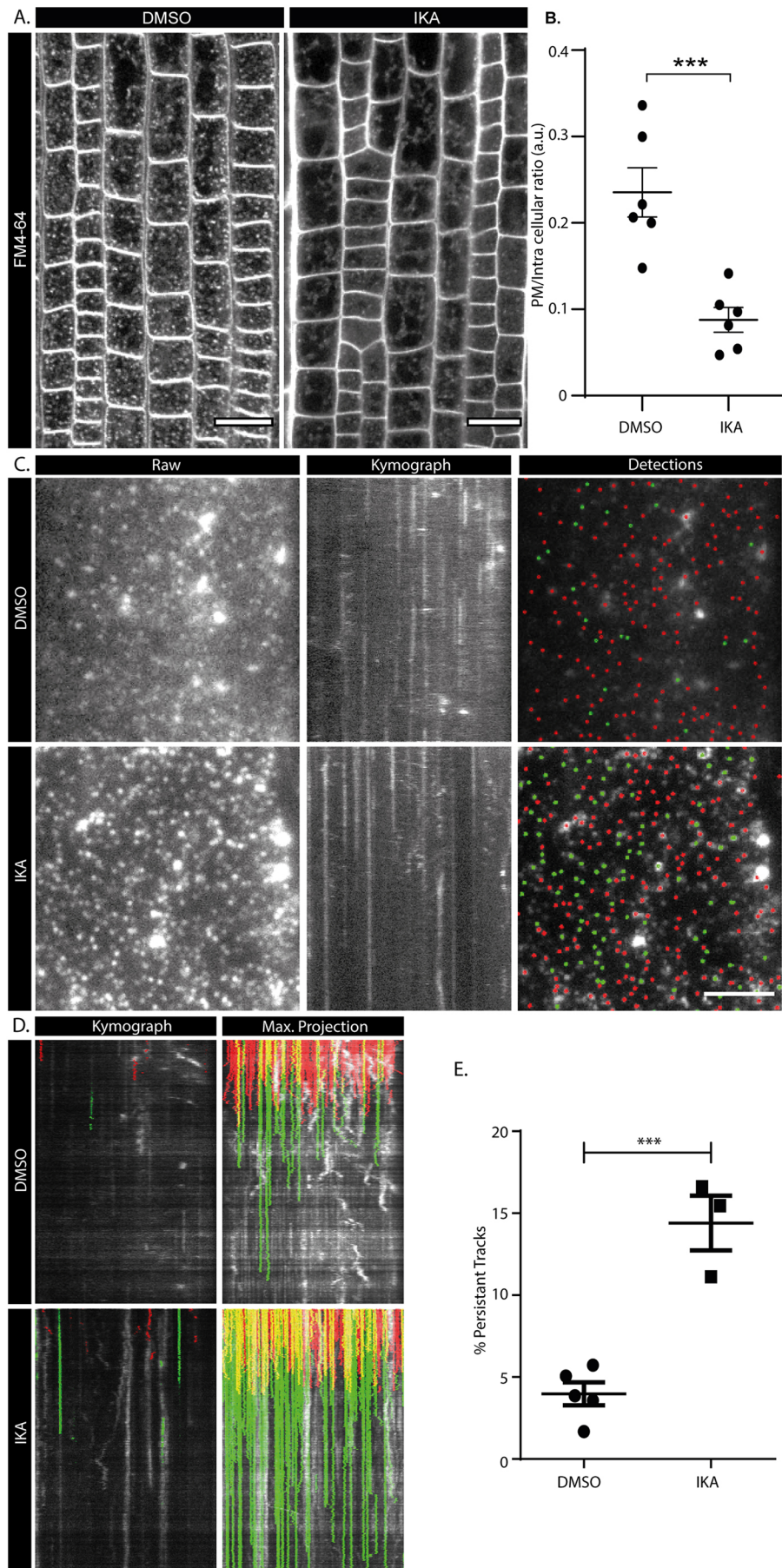


Fig. 7. Inhibition of endocytosis by ikarugamycin. (A) Representative confocal images of epidermal root cells incubated with FM4-64 in the presence of mock (DMSO) or IKA (30 μ M) treatment. (B) Quantification of the membrane uptake. Plots indicate mean \pm s.e.m. For DMSO, $n=6$ independent seedlings, 170 cells; for IKA, $n=6$ independent seedlings, 144 cells. $***P=0.0009$ (t -test). (C) Example TIRF-M images and kymographs corresponding to mock- (DMSO) or IKA- (30 μ M, 15 min) treated root cells expressing CLC2-GFP. The detection panel highlights tracks that are present within the first 100 frames of the movie. (D) Green and red denote tracks that do or do not persist over 100 frames (100 s), respectively, relative to the beginning frame (start of sequence). (E) Data from multiple experiments are combined and plotted as the percentage of tracks within the first 100 frames that persist for this duration. Plots indicate mean \pm s.e.m. For DMSO, $n=5$ cells from independent roots, 3861 tracks; for IKA, $n=3$ cells from independent roots, 3614 tracks. $***P=0.0005$ (t -test). Scale bars: 20 μ m (A), 5 μ m (C).

roots, 35 s in hypocotyl) (Narasimhan et al., 2020). As the output is a relative metric (the percentage of persistent tracks versus total tracks within the first 100 s), the effectiveness of different inhibitors on the process of CME in wild-type plants can be compared. For example, we found that the CME inhibitory effects of IKA are stronger than those of Dyngo 4a (Fig. 7C-E; Fig. S4).

DISCUSSION AND CONCLUSIONS

Plant CME is vital to many key physiological processes, but it remains largely uncharacterized at multiple scales compared to other model systems. Significant progress has been made in the last decade to enhance our understanding of CME, which has been enabled through the identification of evolutionarily conserved and plant-specific factors involved in CME. Further in-depth analysis of the temporal and spatial dynamics of the protein–protein and protein–membrane interactions necessary for the initiation, maturation and release of CCV during CME requires a comprehensive set of tools optimized for the direct, quantitative and unbiased examination of plant CME at multiple scales. Here, we present refined imaging and analysis protocols that allow the quantifiable characterization of plant CME at the ultrastructural, single CME event and tissue levels. The aim is to provide the plant community working on endocytosis in many different physiological and developmental contexts with a standardized set of tools enabling quantitative and directly comparative studies.

Another important area for the standardization of plant CME investigations is the highlighting of robust EAP antibodies. To date, use of a variety of antibodies has led to key insights regarding the interactions and localization of EAPs in both pull-down assays and immunohistochemical staining of plant tissues (Dejonghe et al., 2019; Dhonukshe et al., 2007; di Rubbo et al., 2013; Gadeyne et al., 2014; Gao et al., 2019). Therefore, to broaden the standardization of plant CME tools to include antibodies, researchers are encouraged to submit their routinely used antibodies to online databases such as Antibodypedia (Björling and Uhlén, 2008).

Although further work is required to characterize and develop more specific pharmacological and genetic tools for interrogation of each individual step of plant CME, combination of the presented imaging methods with pharmacological and genetic manipulation tools will enable and accelerate our understanding of plant CME. Moreover, the further development of super-resolution imaging for plants, combined with computational analysis tools will further our ability to improve the precise characterization of plant CME.

MATERIALS AND METHODS

Matlab code with additional detailed instructions can be downloaded at doi:10.5281/zenodo.3888519 and will be maintained and updated at www.github.com/ajohnsoncode/plantCmeMethods. Example data can be found at doi:10.5281/zenodo.3888531.

Expanded method 1: SEM visualization of *Arabidopsis* protoplast CCVs using a metal replica of unroofed cells

Here, we present a method that allows visualization of CCVs in *Arabidopsis* protoplast cells [adapted from Dóczi et al. (2011); Svitkina (2007)]. The cells are unroofed and coated with metal to produce a replica of the cell interior, where PM-associated elements can be observed (Fig. 2). By analyzing these samples with SEM, one can directly count the number of CME vesicles and quantify their size, structural arrangement and localization within the cell.

Cell preparation

1. Protoplasts are isolated from 3-day-old *Arabidopsis* suspension culture cells derived from roots (note 1). 25 ml of suspension

culture is initially centrifuged at 527 *g* for 5 min at room temperature (RT).

2. After removing the supernatant, the pelleted cells are resuspended in 25 ml of enzyme solution in growth medium (GM) [2.2 g Murashige and Skoog (MS) powder with vitamins (Duchefa Biochemie, #M0222), 15.25 g glucose, 15.25 g mannitol, H₂O to 500 ml; pH 5.5 adjusted with KOH] supplemented with 1% cellulose (Yakult) and 0.2% Macerozyme (Yakult) (note 2). The whole resuspension is then incubated for 4 h in the dark with gentle agitation to digest the cell wall.
3. Once the majority of the cells are round, the cells are washed twice and spun at 337 *g* and 234 *g* for 5 min each with GM (note 3).
4. After removing the supernatant, cells are resuspended in sucrose buffer (4.4 g/l of MS powder and 0.28 M sucrose; pH 5.5 adjusted with KOH) and centrifuged at 150 *g* for 7 min. The protoplasts, which are now suspended on top of the sucrose gradient, are carefully removed with a Pasteur pipette and stored overnight at 4°C.
5. Coverslips for plating the cells are prepared as follows:
 - a. 12 mm diameter glass coverslips are washed in absolute ethanol and air dried.
 - b. Coverslips are carbon coated to a thickness of 10 nm using the ACE600 high-vacuum coating device (Leica Microsystems).
 - c. Coverslips are coated with poly-L-lysine (Sigma) at 4°C overnight.
 - d. Coverslips are washed with ddH₂O to remove any excess poly-L-lysine.
6. Protoplasts prepared are plated on the coated coverslips and incubated at RT for 4 h to allow the cells to adhere to the coverslips.
7. Plated protoplasts together with the coverslips are spun at 150 *g* for 5 min to further aid cell adhesion.

Unroofing of cells

8. Excess protoplasts are removed gently from the coverslips using a Pasteur pipette. Samples are washed briefly with PBS (without Ca²⁺ and Mg²⁺) and equilibrated to RT in the same dish.
9. Extraction solution [(2 μM phalloidin, 1% (w/v) Triton X-100 and 1% (w/v) polyethylene glycol (PEG; MW 20,000) in PEM buffer (100 mM PIPES free acid, 1 mM MgCl₂, 1 mM EGTA; pH 6.9 adjusted with KOH)] was equilibrated to RT and applied for 4 min at RT with gentle agitation.
10. Samples are washed three times in PEM buffer plus 1% PEG for 1 min each at RT.
11. Samples are fixed with 2% (v/v) glutaraldehyde in 0.1 M phosphate buffer, pH 7.4, for 20 min at RT and then washed three times in ddH₂O for 5 min each at RT.
12. Samples are further incubated with 0.1% (w/v) tannic acid in water for 20 min at RT and then washed twice with excess of ddH₂O for 5 min each.
13. Samples are treated with 0.2% (w/v) uranyl acetate in water for 20 min at RT and then washed twice with ddH₂O.

Dehydration

14. Lens tissue with loosely arranged fibers (Kimberly-Clark) are cut into squares, a little larger than the diameter of sample holders for critical point drying (CPD; round wire baskets, Leica Microsystems).
15. CPD sample holders are placed in a glass beaker filled with distilled water and a piece of lens tissue is put at the bottom of each holder. A coverslip with cells facing up is then placed on the lens tissue and covered with another piece of lens tissue. This loading procedure of alternating coverslips and lens tissue is continued until the holders are filled. Samples are always kept in water.
16. Sample holders are placed on a homemade standing device for quick transfer from glass beaker to glass beaker with increasing concentrations of ethanol in water (10, 20, 40, 60, 80, 96 and 3×100%). Incubation times are 5 min each at RT. The standing device is constructed in such a way that a magnetic rod fits under the mounting plate for sample holders and the solution can be kept under constant agitation on a magnetic stirrer.

Critical point drying and coating

17. The chamber of the CPD device EM CPD 30 (Leica Microsystems) is filled with absolute ethanol, just sufficient to cover the CPD holder. The holder is then placed in the ethanol bath and the CPD operated according to the manufacturer's instructions.
18. Samples are fixed onto SEM specimen mounts using carbon conductive adhesive tabs (diameter 12 mm) and coated with gold or platinum to a thickness of 5 nm by rotary shadowing at a 45° angle using an ACE600 coating device.

Imaging

19. Samples are examined in a FE-SEM Merlin Compact VP (Zeiss) and imaged with an In-lens Duo detector (SE and BSE imaging) at an accelerating voltage of 0.5 to 5 kV.

Analysis (example analysis to determine the size of the CCVs)

20. The image is opened in Fiji/ImageJ (NIH).
21. The scale of the image is set to the correct calibration (analysis menu>'set scale').
22. Regions of interest (ROIs) are created on the structures/features you want to measure using the line tool. Press 't' to add them to the ROI manager. When all the ROIs are made, it is important to save them, and the ROIs can be measured by pressing the 'measure' button. Results are copied and pasted into Excel for further analysis (Fig. S1).

Notes and considerations

1. The specific cells used here are Col-0 *Arabidopsis* root-derived suspension cultures, and were gifted to us by Eva Kondorosi (Gif-sur-Yvette, France). They were maintained and grown in suspension medium (SM) [4.25 g/l MS salts, 30 g/l sucrose, 0.250 mg 2,4-D, 0.015 mg kinetin and 2 ml vitamin B5 stock (100 ml stock contains 0.1 g nicotinic acid, 0.1 g pyridoxine HCl, 1 g thiamine HCl and 10 g myo-inositol) at pH 5.7].
2. The enzyme solution and the GM buffer are filter sterilized and stored at 4°C.
3. Centrifugations from step 3 are carried out at RT with no breaks to avoid damaging digested cells.

Expanded method 2: Cell surface TIRF-M of *Arabidopsis* root epidermal cells

Here, we present a method that allows the automated direct examination of EAPs and single events of CME on the PM. Briefly, plants expressing fluorescently labeled EAPs are imaged over time using a microscopy approach that directly examines the PM (Fig. 3). Automated analysis detects and tracks the proteins over the duration of the movie. The detections are unbiased and based upon parameters of the experimental setup used; quantifiable outputs include the lifetimes (mean and distribution), density and mean fluorescent profiles for both single- (Fig. 4) and dual-channel experiments (Fig. 5). Using dual-channel data, a departure assay is conducted, which produces a recruitment profile of the protein of interest for single events of CME. This provides an imaging and analysis method to determine precisely the physiological temporal dynamics of proteins in plant CME.

Tissue preparation

1. Seeds expressing a suitable CME marker (Table S2) are sterilized and sown in a row at the top of AM+ 1% sucrose agar plates, spaced at least 1 cm apart.
2. Plates are incubated for 2 days at 4°C in darkness.
3. Plates are transferred to growth rooms at 21°C, with 16 and 8 h light and dark cycles, and grown for 5-7 days (note 1). It is crucial that the plates are slightly tilted backwards; if the plates are too vertical then

the seedlings grow too many hairs to enable flat contact with the coverslip (Fig. S7, photo 1).

Coverslip preparation

4. During this incubation period, coverslips of 24×50 mm, thickness 1.5 (VWR #631-0147) are prepared and cleaned as follows (note 2):
 - a. Coverslips are placed in a coverslip holder (Sigma, Wash-N-Dry) and washed in 'cleaning' solution [0.01% (w/v) Decon 90, NaOH 100 mM] in a 250 ml beaker (Fig. S7, photo 2) and incubated for 15 min.
 - b. Coverslips are cleaned using lens tissue (GE Healthcare, Whatman) and placed back into the coverslip holder.
 - c. Coverslips are washed again in cleaning solution for a further 15 min.
 - d. Coverslips are washed at least five times in ddH₂O, for 5 min each, until there are no more detergent bubbles in the solution.
 - e. Coverslips are washed twice with 100% ethanol for 5 min.
 - f. Coverslips are removed from the washing beaker and allowed to air dry (this is normally done in a flow hood to speed up drying and ensure that the coverslips remain sterile). Ensure that the coverslips are separated to allow each one to dry (Fig. S7, photo 3).
 - g. Coverslips are washed in acetone, for at least 5 min and then air dried and stored in a sterile manner. Coverslips should not be stored for longer than 3 weeks.

Sample preparation

5. The root of interest is cut about 1 cm from the tip of the root and gently laid flat on a microscopy slide (76×26 mm; Carl Roth #H869) (note 3).
6. The root is covered with an excess of experimental medium (~60 µl) and a precleaned coverslip is slowly placed on top of the root, ensuring there are no bubbles created and that the root stays in the middle of the coverslip (Fig. S7, photos 4-5).
7. Excess medium is aspirated away (by tissue or pipette), resulting in the coverslip providing a small amount of pressure to ensure that the root is in direct contact with the coverslip (Fig. S7, photo 6). It is important not to apply any additional force, as it will damage the tissue structure.
8. The coverslip is sealed onto the slide by applying nail polish, to prevent the medium evaporating away. Start with the corners and sides, then seal the whole coverslip and allow to dry (Fig. S7, photos 7-9).

TIRF-M imaging

9. The slide is mounted onto the TIRF microscope and the appropriate settings for the system and fluorophores are used. Typically, an 100×1.49 NA oil immersion objective (note 4) is used and 488 nm and 561 nm lasers for green or red fluorescent proteins.
10. Cells in the elongation zone, determined to be 6-10 cells away from the end of the lateral root cap (Fig. 3A), are imaged. This is crucial for obtaining reproducible results (note 5).
11. Time-lapse movies are acquired typically at 1 frame per second, for either 5 or 10 min total duration (301 or 601 frames in total) (note 6). Dual-channel images are captured sequentially.

Analysis

12. Movies are opened in ImageJ (NIH) and cropped to include only the area of interest.
13. For single-channel analysis, *Arabidopsis thaliana* Col-0, plants expressing pCLC2::CLC2-GFP (AT2G40060) (Konopka et al., 2008) were used in this study:
 - a. singChan_cellSurfaceAnalysis is run in Matlab (note 7) (for further details on how to use this program, see the cell surface analysis instruction PDF).

- b. To combine data from multiple experiments, combineSingChanData is run in Matlab (for further details on how to use this program, see the cell surface analysis instruction PDF).
14. For the dual-channel departure analysis, *Arabidopsis thaliana tplate*, plants expressing pLAT52::TPLATE-GFP (AT3G01780)×pRPS5::CLC2-RFP (Gadeyne et al., 2014) were used in this study:
 - a. dualChan_cellSurfaceAnalysis is run in Matlab (note 8) (for further details on how to use this program, see the analysis instruction PDF).
 - b. To combine data from multiple experiments, combineDualChanData is run in Matlab (for further details on how to use this program, see the cell surface analysis instruction PDF).

Notes and considerations

1. Different durations of growth period affect the location of a good TIRF region in the root (note 5).
2. It is essential to clean the coverslips to remove any possibility of disruptions in the optical pathway.
3. Roots are imaged one at a time to maximize the chances of having a perfectly flat cell for imaging.
4. TIRF-M was conducted on an Olympus IX83 inverted microscope equipped with a Cell[^]TIRF module using an OLYMPUS Upo N 100×1.49 Oil TIRF objective. Wavelengths of 488 and 561 nm were used to stimulate GFP and RFP signals; a quad line beam splitter emission filter (Chroma) was used in combination with an EM-CCD camera (Hamamatsu) to acquire the data.
5. The location of imaging is crucial for producing good TIRF-M images and for reproducible results (Fig. 3A). This is because it has been reported that the kinetics of CME change with the different stages of development in the roots (Konopka et al., 2008). Also, cells in the elongation zone are used for imaging as they normally lie flat on the coverslip, which allows distortion-free TIRF imaging of the roots. It is important to pick a cell that presents a uniform field of illumination across the sample and is free from large autofluorescent structures (Fig. S2). It is also essential to image cells located at the same distance from the root tip for comparison between genotypes or conditions. The end of the lateral root cap can be used as a reference (Fig. 3).
6. The resultant lifetime is highly dependent upon the frame rate used to image. This is due to the high level of short transient visits of EAPs to the cell surface in plants; therefore, a rapid acquisition rate (<1 Hz) includes many more of these events than a slow rate (Johnson and Vert, 2017).
7. Particle detection and tracking of the EAPs is conducted using just the detection and tracking programs of the cmeAnalysis package (Aguet et al., 2013), as the further filtering in this package is highly optimized for mammalian CME events and not suitable for plant CME analysis. Although there are other automated detection systems available (Loerke et al., 2009; Tinevez et al., 2017), the detection method presented here outperforms manual and other programs in robustness and sensitivity (Mettlen and Danuser, 2014). The tracks are filtered for analysis so that they only include tracks absent from the first and last 10 frames of the movie, tracks not within 10 pixels of the edge of the movie and tracks that persist long than 5 frames. The lifetime is then calculated as the mean of all the combined tracks. The density is generated by imposing a 100×100 pixel ROI in the center of the movie, and the mean number of valid tracks is calculated over 100 frames (where the time range of frames used is 50 before the middle time lapse image to 50 after the middle time lapse image). This means that the image of the cell must be larger than this 100×100 pixel ROI and the duration must be 101 or more frames. To test for significance, data from multiple experiments are combined and subjected to an unpaired, parametric two-tailed *t*-test. The mean profile is generated by combining and normalizing all the intensity profiles of tracks that have a lifetime within the range of mean lifetime±3 frames and aligned to their termination.
8. Dual-channel analysis is conducted using a primary channel/secondary channel approach. The tracks in the primary channel are

detected, tracked and filtered as in the single-channel analysis (note 7). Further filtering is conducted whereby the master track must have a significant signal in the secondary channel that persists for more than five frames. The filtered tracks are then used to calculate the mean lifetime and density as in note 7. The mean profile is generated in the same way as in note 7 but, additionally, the slave profiles are normalized and both the primary and secondary profiles are plotted.

9. These analysis systems have been tested and found to work on spinning disk PM data, but strong levels of fluorophore expression are required (Wang et al., 2020).

Expanded method 3: FM 4-64 uptake assay in *Arabidopsis* root epidermal cells

Here, we present a method that allows rapid assessment of the overall efficiency of internalization of the PM. Briefly, by determining the amount of FM dye internalized into the cell over a certain time period, one can assess the overall efficiency of endocytosis in a whole seedling (Fig. 6). By combining this approach with pharmacological agents (Table S3) or genetically altered plants (Table S4), one can directly assess the effect of such experimental manipulation.

Intact *Arabidopsis* seedlings are pre-incubated with either control or treatment solutions, then incubated with FM4-64 in either control or treatment conditions. Once the samples are mounted onto a microscopy slide, images are obtained using a confocal microscope (Fig. 6D). Once samples images are acquired (Fig. 6E), the experiments can be quantified using our semi-automated Matlab analysis system. Cells are segmented using a user-entered threshold value and then a ratio between the PM and intracellular signal is determined (Fig. 6F,G). This provides the direct assessment of PM internalization (using a novel semi-automated analysis system) and indicates the potential effects of CME disruption.

Tissue preparation

1. 10-20 sterilized Col-0 seeds are plated onto AM+ and 1% sucrose agar plates, with ample space for the roots to grow vertically.
2. Plates are incubated for 2 days at 4°C in darkness.
3. Plates are incubated in growth rooms for 5-7 days at 21°C, with 16 and 8 h light and dark cycles.

Treatment and imaging

4. Seedlings are incubated in 2 ml AM+ broth supplemented with 1% sucrose and subjected to either mock or a chemical treatment for 15 min in a six-well cell plate (note 1). Several seedlings can be processed and imaged together. To avoid disruption of the samples due to static interaction of the roots with the plate it is recommended that not more than two seedlings are incubated at the same time.
5. Seedlings are incubated in 2 ml AM+ broth supplemented with 1% sucrose and subjected to either mock or a chemical treatment and 2 μM FM dye (note 2), for 15 min (note 3) in a six-well plate.
6. Seedlings are washed gently twice by dipping them in a clean well containing 2 ml of the required experimental medium (without FM4-64 to reduce background signal from weakly bound FM dye).
7. Seedlings are transferred onto a microscope slide (76×26 mm; Carl Roth #H869) covered in experimental medium and then carefully covered with a coverslip (24×50 mm, thickness 1.5; VWR #631-0147), ensuring that there are no bubbles and that the root remains undamaged (Fig. S7, photos 10-12).
8. Seedlings are imaged with a confocal microscope. Here, we made use of an inverted 800 or 880 Zeiss confocal microscope, equipped with a 40×1.2 NA water emersion objective. The elongation zone (note 4) of the root epidermis is imaged, and a small Z-stack is taken that captures the signals from both the cell wall and the inner part of the sample.

Analysis

9. The z-plane that shows clean signal from the lateral sides of the FM-stained PM and no clear sign of organelles blocking the

cytoplasm region in which FM dye could be present is chosen for analysis (Fig. S6A).

10. The single plane is saved as a TIF file using ImageJ (NIH).
11. In Matab, the fmUptakeAnalysis is initiated (for details on how to use this program, see the fmAnalysis PDF manual).
12. When prompted, enter a threshold value (note 5) to attempt to generate a good segmentation of the individual cells. It is crucial to set a threshold that produces the most filled cells (Fig. S6B).
13. Individual segmented cells are selected for analysis by user selection (notes 6 and 7).

Notes and considerations

1. IKA (Abcam; ab143408) is used at 30 μ M for 15 min.
2. FM4-64 (ThermoFisher; T3166) is a 'red' dye, so can be used together with a GFP marker to determine whether a labeled cargo can enter the FM-labeled early endosomes. There are other dyes available (e.g. FM1-43; ThermoFisher, T3163) that emit in the yellow range and function in the same way (Fig. S3). FM4-64 and FM1-43 are used at 2 μ M and incubated for 15 min.
3. Prolonged FM treatment has been reported to be toxic to plant tissues (Meckel et al., 2004), therefore long-term treatments are not advised.
4. The location of cells and region of the plant chosen for analysis are important because different developmental stages of the root have been reported to have different kinetic rates of endocytosis (Konopka et al., 2008).
5. The value entered affects the strength of the image segmentation (Fig. S6). First, a Gaussian filter is applied to the image and then the entered threshold value determines the luminance threshold to binarize the image, which is used to define the PM and intracellular regions.
6. Cells selected should not contain areas where there are clear dark shadows visible inside the cell, as these are most likely organelles deep in the cell that physically exclude FM-containing structures from the cytoplasmic space (Fig. S6A).
7. Selected cells should be separated from the surrounding cells and outlines of badly segmented cells (Fig. S6B). This step can be checked immediately after cell selection.
8. Data from multiple experiments are combined and tested for significance using an unpaired, parametric two tailed *t*-test in GraphPad Prism 6.0. No sample size calculation is conducted.

Expanded method 4: Spot persistence assay

Here, we present a method that allows determination of whether chemical or genetic manipulation of CME significantly disrupts EAPs on the PM. TIRF-M imaging is conducted as detailed in 'Expanded method 2', but with a different analysis system. This is crucial and overcomes the shortcomings of using a standard lifetime measurement to assess the effects of CME inhibitors. The percentage of spots that persist out of the total amount of spots detected within the first 100 frames of the time lapse is calculated (Fig. 7C).

Sample preparation and imaging

Sample preparation and imaging is conducted as described in 'Expanded method 3' (note 1).

Analysis

1. Run singChan_cellSurfaceAnalysis as detailed in 'Expanded method 3' (point 13).
2. Run the persisTest program (for further details on how to use this program, see the cell surface analysis instruction PDF) (note 2)

Notes and considerations

1. The time lapse of the experiment must be over 100 frames, as this is this number of frames used to determine persistence. Typically, the

frame rate of these experiments should be 1 Hz; therefore, 100 frames represents a time point that is over twice the duration of a bone fide CME event in the root (Narasimhan et al., 2020). If the frame rate is changed, it should cover a duration greater than this. However, if the frame rate is too quick, then the persistent spots are subjected to more bleaching effects.

2. The detection and tracking of spots in the movies are made in the same way as for 'Expanded method 3'. However, tracks present in the first and last frames are still retained for analysis, and the duration of track measures is greater than 24 frames (this is the mean lifetime of single-channel CLC2 and thus filters additional noise from use of an inhibitor). Then, all the frames that are present at the start of the movie are counted and the percentage of tracks that persist longer than 100 frames is calculated.
3. To test for significance, data from multiple experiments are combined and subjected to an unpaired, parametric two-tailed *t*-test. No sample size calculation is conducted.
4. Inhibitor experiments used IKA (Abcam; ab143408) and Dyngo-4a (Abcam; ab120689) at 30 μ M and with a 15 min incubation.

Acknowledgements

This paper is dedicated to the memory of Christien Merrifield. He pioneered quantitative imaging approaches in mammalian CME and his mentorship inspired the development of all the analysis methods presented here. His joy in research, pure scientific curiosity and microscopy excellence remain a constant inspiration. We thank Daniel Van Damme for giving us the CLC2-GFP×TPLATE-TagRFP plants used in this article. We further thank the Scientific Service Units at IST Austria, specifically the Electron Microscopy Facility, for technical assistance (in particular Vanessa Zheden) and the Biolmaging Facility for access to equipment.

Competing interests

The authors declare no competing or financial interests.

Author contributions

Conceptualization: A.J., J.F.; Methodology: A.J., W.A.K., M.N., G.V.; Software: A.J.; Formal analysis: A.J., N.G.; Investigation: A.J., N.G., W.A.K., M.N.; Resources: S.Y.B.; Writing - original draft: A.J., J.F.; Writing - review & editing: A.J., N.G., W.A.K., M.N., G.V., S.Y.B., J.F.; Supervision: J.F.; Funding acquisition: J.F.

Funding

A.J. is supported by funding from the Austrian Science Fund (FWF) (I3630B25 to J.F.). N.G. is supported by European Union's Horizon 2020 Framework Programme under the Marie Skłodowska-Curie Grant Agreement No. 665385. This work was partially supported by an award from the National Science Foundation to S.Y.B. (award no. 1614915).

Data availability

Raw data presented in this study is available at doi:10.5281/zenodo.3888544.

Supplementary information

Supplementary information available online at <https://jcs.biologists.org/lookup/doi/10.1242/jcs.248062.supplemental>

Peer review history

The peer review history is available online at <https://jcs.biologists.org/lookup/doi/10.1242/jcs.248062.reviewer-comments.pdf>

References

- Adamowski, M., Narasimhan, M., Kania, U., Glanc, M., DE Jaeger, G. and Friml, J. (2018). A functional study of AUXILIN-LIKE1 and 2, two putative clathrin uncoating factors in arabidopsis. *Plant Cell* **30**, 700-716. doi:10.1105/tpc.17.00785
- Aguet, F., Antonescu, C. N., Mettlen, M., Schmid, S. L. and Danuser, G. (2013). Advances in analysis of low signal-to-noise images link dynamin and AP2 to the functions of an endocytic checkpoint. *Dev. Cell* **26**, 279-291. doi:10.1016/j.devcel.2013.06.019
- Axelrod, D. (2001). Total internal reflection fluorescence microscopy in cell biology. *Traffic* **2**, 764-774. doi:10.1034/j.1600-0854.2001.21104.x
- Banbury, D. N., Oakley, J. D., Sessions, R. B. and Banting, G. (2003). Tyrphostin A23 inhibits internalization of the transferrin receptor by perturbing the interaction between tyrosine motifs and the medium chain subunit of the AP-2 adaptor complex. *J. Biol. Chem.* **278**, 12022-12028. doi:10.1074/jbc.M211966200

- Bandmann, V., Müller, J. D., Köhler, T. and Homann, U. (2012). Uptake of fluorescent nano beads into BY2-cells involves clathrin-dependent and clathrin-independent endocytosis. *FEBS Lett.* **586**, 3626-3632. doi:10.1016/j.febslet.2012.08.008
- Barberon, M., Zelazny, E., Robert, S., Conéjéro, G., Curie, C., Friml, J. and Vert, G. (2011). Monoubiquitin-dependent endocytosis of the iron-regulated transporter 1 (IRT1) transporter controls iron uptake in plants. *Proc. Natl. Acad. Sci. USA* **108**, E450-E458. doi:10.1073/pnas.1100659108
- Barberon, M., Dubeaux, G., Kolb, C., Isono, E., Zelazny, E. and Vert, G. (2014). Polarization of IRON-REGULATED TRANSPORTER 1 (IRT1) to the plant-soil interface plays crucial role in metal homeostasis. *Proc. Natl. Acad. Sci. USA* **111**, 8293-8298. doi:10.1073/pnas.1402262111
- Bashline, L., Li, S., Anderson, C. T., Lei, L. and Gu, Y. (2013). The endocytosis of cellulose synthase in Arabidopsis is dependent on μ 2, a clathrin-mediated endocytosis adaptin. *Plant Physiol.* **163**, 150-160. doi:10.1104/pp.113.221234
- Beck, M., Zhou, J., Faulkner, C., Maclean, D. and Robatzek, S. (2012). Spatio-temporal cellular dynamics of the Arabidopsis flagellin receptor reveal activation status-dependent endosomal sorting. *Plant Cell* **24**, 4205-4219. doi:10.1105/tpc.112.100263
- Betz, W. J., Mao, F. and Smith, C. B. (1996). Imaging exocytosis and endocytosis. *Curr. Opin. Neurobiol.* **6**, 365-371. doi:10.1016/S0959-4388(96)80121-8
- Bitsikas, V., Corrêa, I. R., Jr. and Nichols, B. J. (2014). Clathrin-independent pathways do not contribute significantly to endocytic flux. *eLife* **3**, e03970. doi:10.7554/eLife.05256
- Björling, E. and Uhlén, M. (2008). Antibodypedia, a portal for sharing antibody and antigen validation data. *Mol. Cell. Proteomics* **7**, 2028-2037. doi:10.1074/mcp.M800264-MCP200
- Botte, S., Talbot, C., Boutte, Y., Catrice, O., Read, N. D. and Satiat-Jeunemaitre, B. (2004). FM-dyes as experimental probes for dissecting vesicle trafficking in living plant cells. *J. Microsc.* **214**, 159-173. doi:10.1111/j.0022-2720.2004.01348.x
- Bonnett, H. T. and Newcomb, E. H. (1966). Coated vesicles and other cytoplasmic components of growing root hairs of radish. *Protoplasma* **62**, 59-75. doi:10.1007/BF01254633
- Cao, Y., He, Q., Qi, Z., Zhang, Y., Lu, L., Xue, J., Li, J. and Li, R. (2020). Dynamics and endocytosis of Flot1 in Arabidopsis require CPI1 function. *Int. J. Mol. Sci.* **21**, 1552. doi:10.3390/ijms21051552
- Chen, T., Ji, D. and Tian, S. (2018). Variable-angle epifluorescence microscopy characterizes protein dynamics in the vicinity of plasma membrane in plant cells. *BMC Plant Biol.* **18**, 43. doi:10.1186/s12870-018-1246-0
- Cheung, G. and Cousin, M. A. (2011). Quantitative analysis of synaptic vesicle pool replenishment in cultured cerebellar granule neurons using FM dyes. *J. Vis. Exp.* **57**, e3143. doi:10.3791/3143
- de Jonge, N., Peckys, D. B., Kremers, G. J. and Piston, D. W. (2009). Electron microscopy of whole cells in liquid with nanometer resolution. *Proc. Natl. Acad. Sci. USA* **106**, 2159-2164. doi:10.1073/pnas.0809567106
- Dejonghe, W., Kuenen, S., Mylle, E., Vasileva, M., Keech, O., Viotti, C., Swerts, J., Fendrych, M., Ortiz-Moreno, F. A., Mishev, K. et al. (2016). Mitochondrial uncouplers inhibit clathrin-mediated endocytosis largely through cytoplasmic acidification. *Nat. Commun.* **7**, 11710. doi:10.1038/ncomms11710
- Dejonghe, W., Sharma, I., Denoo, B., DE Munck, S., Lu, Q., Mishev, K., Bulut, H., Mylle, E., DE Rycke, R., Vasileva, M. et al. (2019). Disruption of endocytosis through chemical inhibition of clathrin heavy chain function. *Nat. Chem. Biol.* **15**, 641-649. doi:10.1038/s41589-019-0262-1
- Dhonukshe, P., Aniento, F., Hwang, I., Robinson, D. G., Mravec, J., Stierhof, Y.-D. and Friml, J. (2007). Clathrin-mediated constitutive endocytosis of PIN auxin efflux carriers in Arabidopsis. *Curr. Biol.* **17**, 520-527. doi:10.1016/j.cub.2007.01.052
- di Rubbo, S., Irani, N. G., Kim, S. Y., Xu, Z.-Y., Gadeyne, A., Dejonghe, W., Vanhoutte, I., Persiau, G., Eeckhout, D., Simon, S. et al. (2013). The clathrin adaptor complex AP-2 mediates endocytosis of brassinosteroid insensitive1 in Arabidopsis. *Plant Cell* **25**, 2986-2997. doi:10.1105/tpc.113.114058
- Dóczy, R., Hatzimasoura, E. and Bögre, L. (2011). Mitogen-activated protein kinase activity and reporter gene assays in plants. *Methods Mol. Biol.* **779**, 79-92. doi:10.1007/978-1-61779-264-9_5
- Doyon, J. B., Zeidler, B., Cheng, J., Cheng, A. T., Cherone, J. M., Santiago, Y., Lee, A. H., Vo, T. D., Doyon, Y., Miller, J. C. et al. (2011). Rapid and efficient clathrin-mediated endocytosis revealed in genome-edited mammalian cells. *Nat. Cell Biol.* **13**, 331-337. doi:10.1038/ncb2175
- Dutta, D. and Donaldson, J. G. (2012). Search for inhibitors of endocytosis: intended specificity and unintended consequences. *Cell Logist.* **2**, 203-208. doi:10.4161/cl.23967
- Elkin, S. R., Oswald, N. W., Reed, D. K., Mettlen, M., Macmillan, J. B. and Schmid, S. L. (2016). Ikarugamycin: a natural product inhibitor of clathrin-mediated endocytosis. *Traffic* **17**, 1139-1149. doi:10.1111/tra.12425
- Fan, L., Hao, H., Xue, Y., Zhang, L., Song, K., Ding, Z., Botella, M. A., Wang, H. and Lin, J. (2013). Dynamic analysis of Arabidopsis AP2 sigma subunit reveals a key role in clathrin-mediated endocytosis and plant development. *Development* **140**, 3826-3837. doi:10.1242/dev.095711
- Fotin, A., Cheng, Y., Grigorieff, N., Walz, T., Harrison, S. C. and Kirchhausen, T. (2004). Structure of an auxilin-bound clathrin coat and its implications for the mechanism of uncoating. *Nature* **432**, 649-653. doi:10.1038/nature03078
- Fujimoto, M., Arimura, S., Ueda, T., Takanashi, H., Hayashi, Y., Nakano, A. and Tsutsumi, N. (2010). Arabidopsis dynamin-related proteins DRP2B and DRP1A participate together in clathrin-coated vesicle formation during endocytosis. *Proc. Natl. Acad. Sci. USA* **107**, 6094-6099. doi:10.1073/pnas.0913562107
- Gadeyne, A., Sánchez-Rodríguez, C., Vanneste, S., di Rubbo, S., Zauber, H., Vanneste, K., van Leene, J., de Winne, N., Eeckhout, D., Persiau, G. et al. (2014). The TPLATE adaptor complex drives clathrin-mediated endocytosis in plants. *Cell* **156**, 691-704. doi:10.1016/j.cell.2014.01.039
- Gao, J., Chaudhary, A., Vaddepalli, P., Nagel, M.-K., Isono, E. and Schneitz, K. (2019). Arabidopsis receptor kinase STRUBBELIG undergoes clathrin-dependent endocytosis. *J. Exp. Bot.* **70**, 3881-3894. doi:10.1093/jxb/erz190
- Geldner, N., Friml, J., Stierhof, Y.-D., Jürgens, G. and Palme, K. (2001). Auxin transport inhibitors block PIN1 cycling and vesicle trafficking. *Nature* **413**, 425-428. doi:10.1038/35096571
- Gifford, M. L., Robertson, F. C., Soares, D. C. and Ingram, G. C. (2005). ARABIDOPSIS CRINKLY4 function, internalization, and turnover are dependent on the extracellular crinkly repeat domain. *Plant Cell* **17**, 1154-1166. doi:10.1105/tpc.104.029975
- Grebe, M., Xu, J., Möbius, W., Ueda, T., Nakano, A., Geuze, H. J., Rook, M. B. and Scheres, B. (2003). Arabidopsis sterol endocytosis involves actin-mediated trafficking via ARA6-positive early endosomes. *Curr. Biol.* **13**, 1378-1387. doi:10.1016/S0960-9822(03)00538-4
- Gurskaya, N. G., Verkhusha, V. V., Shcheglov, A. S., Staroverov, D. B., Khepurnykh, T. V., Fradkov, A. F., Lukyanov, S. and Lukyanov, K. A. (2006). Engineering of a monomeric green-to-red photoactivatable fluorescent protein induced by blue light. *Nat. Biotechnol.* **24**, 461-465. doi:10.1038/nbt1191
- Helms, J. B. and Rothman, J. E. (1992). Inhibition by brefeldin A of a Golgi membrane enzyme that catalyzes exchange of guanine nucleotide bound to ARF. *Nature* **360**, 352-354. doi:10.1038/360352a0
- Henkel, A. W., Lubke, J. and Betz, W. J. (1996). FM1-43 dye ultrastructural localization in and release from frog motor nerve terminals. *Proc. Natl. Acad. Sci. USA* **93**, 1918-1923. doi:10.1073/pnas.93.5.1918
- Heuser, J. (1980). Three-dimensional visualization of coated vesicle formation in fibroblasts. *J. Cell Biol.* **84**, 560-583. doi:10.1083/jcb.84.3.560
- Higaki, T. (2015). Real-time imaging of plant cell surface dynamics with variable-angle epifluorescence microscopy. *J. Vis. Exp.* **106**, e53437. doi:10.3791/53437
- Hunter, K., Kimura, S., Rokka, A., Tran, H. C., Toyota, M., Kukkonen, J. P. and Wrzaczek, M. (2019). CRK2 enhances salt tolerance by regulating callose deposition in connection with PLD α 1. *Plant Physiol.* **180**, 2004-2021. doi:10.1104/pp.19.00560
- Ito, E., Fujimoto, M., Ebine, K., Uemura, T., Ueda, T. and Nakano, A. (2012). Dynamic behavior of clathrin in Arabidopsis thaliana unveiled by live imaging. *Plant J.* **69**, 204-216. doi:10.1111/j.1365-313X.2011.04782.x
- Jásik, J., Bokor, B., Stuchlík, S., Mičičeta, K., Turňa, J. and Schmelzer, E. (2016). Effects of Auxins on PIN-FORMED2 (PIN2) dynamics are not mediated by inhibiting PIN2 endocytosis. *Plant Physiol.* **172**, 1019-1031. doi:10.1104/pp.16.00563
- Jelínková, A., Malínská, K., Simon, S., Kleine-Vehn, J., Pařezová, M., Pejchar, P., Kubeš, M., Martinec, J., Friml, J., Zažimalová, E. et al. (2010). Probing plant membranes with FM dyes: tracking, dragging or blocking? *Plant J.* **61**, 883-892. doi:10.1111/j.1365-313X.2009.04102.x
- Johnson, A. and Vert, G. (2017). Single event resolution of plant plasma membrane protein endocytosis by TIRF microscopy. *Front. Plant Sci.* **8**, 612. doi:10.3389/fpls.2017.00612
- Kaksonen, M. and Roux, A. (2018). Mechanisms of clathrin-mediated endocytosis. *Nat. Rev. Mol. Cell Biol.* **19**, 313-326. doi:10.1038/nrm.2017.132
- Kang, B.-H., Rancour, D. M. and Bednarek, S. Y. (2003). The dynamin-like protein ADL1C is essential for plasma membrane maintenance during pollen maturation. *Plant J.* **35**, 1-15. doi:10.1046/j.1365-313X.2003.01775.x
- Karlova, R., Boeren, S., Russinova, E., Aker, J., Vervoort, J. and DE Vries, S. (2006). The Arabidopsis SOMATIC EMBRYOGENESIS RECEPTOR-LIKE KINASE1 protein complex includes BRASSINOSTEROID-INSENSITIVE1. *Plant Cell* **18**, 626-638. doi:10.1105/tpc.105.039412
- Kim, S. Y., Xu, Z.-Y., Song, K., Kim, D. H., Kang, H., Reichardt, I., Sohn, E. J., Friml, J., Jürgens, G. and Hwang, I. (2013). Adaptor protein complex 2-mediated endocytosis is crucial for male reproductive organ development in Arabidopsis. *Plant Cell* **25**, 2970-2985. doi:10.1105/tpc.113.114264
- Kitakura, S., Vanneste, S., Robert, S., Löfke, C., Teichmann, T., Tanaka, H. and Friml, J. (2011). Clathrin mediates endocytosis and polar distribution of PIN auxin transporters in Arabidopsis. *Plant Cell* **23**, 1920-1931. doi:10.1105/tpc.111.083030
- Kleine-Vehn, J., Dhonukshe, P., Sauer, M., Brewer, P. B., Wiśniewska, J., Paciorek, T., Benková, E. and Friml, J. (2008a). ARF GEF-dependent transcytosis and polar delivery of PIN auxin carriers in Arabidopsis. *Curr. Biol.* **18**, 526-531. doi:10.1016/j.cub.2008.03.021
- Kleine-Vehn, J., Langowski, Ł., Wiśniewska, J., Dhonukshe, P., Brewer, P. B. and Friml, J. (2008b). Cellular and molecular requirements for polar PIN targeting and transcytosis in plants. *Mol. Plant* **1**, 1056-1066. doi:10.1093/mp/ssn062

- Konopka, C. A. and Bednarek, S. Y.** (2008). Variable-angle epifluorescence microscopy: a new way to look at protein dynamics in the plant cell cortex. *Plant J.* **53**, 186-196. doi:10.1111/j.1365-313X.2007.03306.x
- Konopka, C. A., Backues, S. K. and Bednarek, S. Y.** (2008). Dynamics of Arabidopsis dynamin-related protein 1C and a clathrin light chain at the plasma membrane. *Plant Cell* **20**, 1363-1380. doi:10.1105/tpc.108.059428
- Kwaaitaal, M. A., DE Vries, S. C. and Russinova, E.** (2005). Arabidopsis thaliana Somatic Embryogenesis Receptor Kinase 1 protein is present in sporophytic and gametophytic cells and undergoes endocytosis. *Protoplasma* **226**, 55-65. doi:10.1007/s00709-005-0111-9
- Lam, B. C.-H., Sage, T. L., Bianchi, F. and Blumwald, E.** (2001). Role of SH3 domain-containing proteins in clathrin-mediated vesicle trafficking in Arabidopsis. *Plant Cell* **13**, 2499-2512. doi:10.1105/tpc.010279
- Lambert, T. J.** (2019). FPbase: a community-editable fluorescent protein database. *Nat. Methods* **16**, 277-278. doi:10.1038/s41592-019-0352-8
- Langhans, M., Förster, S., Helmchen, G. and Robinson, D. G.** (2011). Differential effects of the brefeldin A analogue (6R)-hydroxy-BFA in tobacco and Arabidopsis. *J. Exp. Bot.* **62**, 2949-2957. doi:10.1093/jxb/err007
- Leborgne-Castel, N., Lherminier, J., Der, C., Fromentin, J., Houot, V. and Simon-Plas, F.** (2008). The plant defense elicitor cryptogein stimulates clathrin-mediated endocytosis correlated with reactive oxygen species production in bright yellow-2 tobacco cells. *Plant Physiol.* **146**, 1255-1266. doi:10.1104/pp.107.111716
- Li, R., Liu, P., Wan, Y., Chen, T., Wang, Q., Metzbach, U., Baluška, F., Šamaj, J., Fang, X., Lucas, W. J. et al.** (2012). A membrane microdomain-associated protein, Arabidopsis Flot1, is involved in a clathrin-independent endocytic pathway and is required for seedling development. *Plant Cell* **24**, 2105-2122. doi:10.1105/tpc.112.095695
- Loerke, D., Mettlen, M., Yarar, D., Jaqaman, K., Jaqaman, H., Danuser, G. and Schmid, S. L.** (2009). Cargo and dynamin regulate clathrin-coated pit maturation. *PLoS Biol.* **7**, e17. doi:10.1371/journal.pbio.1000057
- Lu, R., Drubin, D. G. and Sun, Y. D.** (2016). Clathrin-mediated endocytosis in budding yeast at a glance. *J. Cell Sci.* **129**, 1531-1536. doi:10.1242/jcs.182303
- Martins, S., Dohmann, E. M. N., Cayrel, A., Johnson, A., Fischer, W., Pojer, F., Satiat-Jeuemaitre, B., Jallais, Y., Chory, J., Geldner, N. et al.** (2015). Internalization and vacuolar targeting of the brassinosteroid hormone receptor BRI1 are regulated by ubiquitination. *Nat. Commun.* **6**, 6151. doi:10.1038/ncomms7151
- Matheyses, A. L., Simon, S. M. and Rappoport, J. Z.** (2010). Imaging with total internal reflection fluorescence microscopy for the cell biologist. *J. Cell Sci.* **123**, 3621-3628. doi:10.1242/jcs.056218
- Matheyses, A. L., Atkinson, C. E. and Simon, S. M.** (2011). Imaging single endocytic events reveals diversity in clathrin, dynamin and vesicle dynamics. *Traffic* **12**, 1394-1406. doi:10.1111/j.1600-0854.2011.01235.x
- Mazur, E., Gallei, M., Adamowski, M., Han, H., Robert, H. S. and Friml, J.** (2020). Clathrin-mediated trafficking and PIN trafficking are required for auxin canalization and vascular tissue formation in Arabidopsis. *Plant Sci.* **293**, 110414. doi:10.1016/j.plantsci.2020.110414
- Mbengue, M., Bourdais, G., Gervasi, F., Beck, M., Zhou, J., Spallek, T., Bartels, S., Boller, T., Ueda, T., Kuhn, H. et al.** (2016). Clathrin-dependent endocytosis is required for immunity mediated by pattern recognition receptor kinases. *Proc. Natl. Acad. Sci. USA* **113**, 11034-11039. doi:10.1073/pnas.1606004113
- McCluskey, A., Daniel, J. A., Hadzic, G., Chau, N., Clayton, E. L., Mariana, A., Whiting, A., Gorgani, N. N., Lloyd, J., Quan, A. et al.** (2013). Building a better dynasore: the dyngo compounds potently inhibit dynamin and endocytosis. *Traffic* **14**, 1272-1289. doi:10.1111/tra.12119
- McMahon, H. T. and Boucrot, E.** (2011). Molecular mechanism and physiological functions of clathrin-mediated endocytosis. *Nat. Rev. Mol. Cell Biol.* **12**, 517-533. doi:10.1038/nrm3151
- Meckel, T., Hurst, A. C., Thiel, G. and Homann, U.** (2004). Endocytosis against high turgor: intact guard cells of *Vicia faba* constitutively endocytose fluorescently labeled plasma membrane and GFP-tagged K⁺-channel KAT1. *Plant J.* **39**, 182-193. doi:10.1111/j.1365-313X.2004.02119.x
- Merrifield, C. J. and Kaksonen, M.** (2014). Endocytic accessory factors and regulation of clathrin-mediated endocytosis. *Cold Spring Harb. Perspect. Biol.* **6**, a016733. doi:10.1101/cshperspect.a016733
- Merrifield, C. J., Feldman, M. E., Wan, L. and Almers, W.** (2002). Imaging actin and dynamin recruitment during invagination of single clathrin-coated pits. *Nat. Cell Biol.* **4**, 691-698. doi:10.1038/ncb837
- Mettlen, M. and Danuser, G.** (2014). Imaging and modeling the dynamics of clathrin-mediated endocytosis. *Cold Spring Harb. Perspect. Biol.* **6**, a017038. doi:10.1101/cshperspect.a017038
- Moscattelli, A., Ciampolini, F., Rodighiero, S., Onelli, E., Cresti, M., Santo, N. and Idilli, A.** (2007). Distinct endocytic pathways identified in tobacco pollen tubes using charged nanogold. *J. Cell Sci.* **120**, 3804-3819. doi:10.1242/jcs.012138
- Mosso, N., Bläske, T., Nagel, M.-K., Laumann, M. and Isono, E.** (2018). Preparation of clathrin-coated vesicles from Arabidopsis thaliana seedlings. *Front. Plant Sci.* **9**, 1972. doi:10.3389/fpls.2018.01972
- Mueller, V. J., Wienisch, M., Nehring, R. B. and Klingauf, J.** (2004). Monitoring clathrin-mediated endocytosis during synaptic activity. *J. Neurosci.* **24**, 2004-2012. doi:10.1523/JNEUROSCI.4080-03.2004
- Naramoto, S., Kleine-Vehn, J., Robert, S., Fujimoto, M., Dainobu, T., Paciorek, T., Ueda, T., Nakano, A., van Montagu, M. C. E., Fukuda, H. et al.** (2010). ADP-ribosylation factor machinery mediates endocytosis in plant cells. *Proc. Natl. Acad. Sci. USA* **107**, 21890-21895. doi:10.1073/pnas.1016260107
- Naramoto, S., Otegui, M. S., Kutsuna, N., de Ruyck, R., Dainobu, T., Karampelias, M., Fujimoto, M., Feraru, E., Miki, D., Fukuda, H. et al.** (2014). Insights into the localization and function of the membrane trafficking regulator GNOM ARF-GEF at the Golgi apparatus in Arabidopsis. *Plant Cell* **26**, 3062-3076. doi:10.1105/tpc.114.125880
- Narasimhan, M., Johnson, A., Prizak, R., Kaufmann, W. A., Tan, S., Casillas-Peréz, B. and Friml, J.** (2020). Evolutionarily unique mechanistic framework of clathrin-mediated endocytosis in plants. *eLife* **9**, e52067. doi:10.7554/eLife.52067
- Ortiz-Moreno, F. A., Savatin, D. V., Dejonghe, W., Kumar, R., Luo, Y., Adamowski, M., van den Begin, J., Dressano, K., Pereira de Oliveira, G., Zhao, X. et al.** (2016). Danger-associated peptide signaling in Arabidopsis requires clathrin. *Proc. Natl. Acad. Sci. USA* **113**, 11028-11033. doi:10.1073/pnas.1605588113
- Ortiz-Zapater, E., Soriano-Ortega, E., Marcote, M. J., Ortiz-Masiá, D. and Aniento, F.** (2006). Trafficking of the human transferrin receptor in plant cells: effects of tyrostatin A23 and brefeldin A. *Plant J.* **48**, 757-770. doi:10.1111/j.1365-313X.2006.02909.x
- Paciorek, T., Zajímalová, E., Ruthardt, N., Petrášek, J., Stierhof, Y.-D., Kleine-Vehn, J., Morris, D. A., Emans, N., Jürgens, G., Geldner, N. et al.** (2005). Auxin inhibits endocytosis and promotes its own efflux from cells. *Nature* **435**, 1251-1256. doi:10.1038/nature03633
- Picco, A. and Kaksonen, M.** (2018). Quantitative imaging of clathrin-mediated endocytosis. *Curr. Opin. Cell Biol.* **53**, 105-110. doi:10.1016/j.cob.2018.06.005
- Qi, X., Pleskot, R., Irani, N. G. and van Damme, D.** (2018). Meeting report - cellular gateways: expanding the role of endocytosis in plant development. *J. Cell Sci.* **131**, jcs222604. doi:10.1242/jcs.222604
- Reynolds, G. D., August, B. and Bednarek, S. Y.** (2014). Preparation of enriched plant clathrin-coated vesicles by differential and density gradient centrifugation. *Methods Mol. Biol.* **1209**, 163-177. doi:10.1007/978-1-4939-1420-3_13
- Robert, S., Kleine-Vehn, J., Barbez, E., Sauer, M., Paciorek, T., Baster, P., Vanneste, S., Zhang, J., Simon, S., Čovanová, M. et al.** (2010). ABP1 mediates auxin inhibition of clathrin-dependent endocytosis in Arabidopsis. *Cell* **143**, 111-121. doi:10.1016/j.cell.2010.09.027
- Robinson, M. S.** (2015). Forty years of Clathrin-coated vesicles. *Traffic* **16**, 1210-1238. doi:10.1111/tra.12335
- Rosquete, M. R., Worden, N., Ren, G., Sinclair, R. M., Pflieger, S., Salemi, M., Phinney, B. S., Domozych, D., Wilkop, T. and Drakakaki, G.** (2019). ATRAPPC11/ROG2: a role for TRAPPs in maintenance of the plant trans-Golgi network/early endosome organization and function. *Plant Cell* **31**, 1879-1898. doi:10.1105/tpc.19.00110
- Russinova, E., Borst, J.-W., Kwaaitaal, M., Caño-Delgado, A., Yin, Y., Chory, J. and de Vries, S. C.** (2004). Heterodimerization and endocytosis of Arabidopsis brassinosteroid receptors BRI1 and ATRK3 (BAK1). *Plant Cell* **16**, 3216-3229. doi:10.1105/tpc.104.025387
- Safavian, D. and Goring, D. R.** (2013). Secretory activity is rapidly induced in stigmatic papillae by compatible pollen, but inhibited for self-incompatible pollen in the Brassicaceae. *PLoS ONE* **8**, e84286. doi:10.1371/journal.pone.0084286
- Salanekka, Y., Verstraeten, I., Löffke, C., Tabata, K., Naramoto, S., Glanc, M. and Friml, J.** (2018). Gibberellin DELLA signaling targets the retromer complex to redirect protein trafficking to the plasma membrane. *Proc. Natl. Acad. Sci. USA* **115**, 3716-3721. doi:10.1073/pnas.1721760115
- Schmid, S. L.** (2019). A nostalgic look back 40 years after the discovery of receptor-mediated endocytosis. *Mol. Biol. Cell* **30**, 1-3. doi:10.1091/mbc.E18-06-0409
- Sharfman, M., Bar, M., Ehrlich, M., Schuster, S., Melech-Bonfil, S., Ezer, R., Sessa, G. and Avni, A.** (2011). Endosomal signaling of the tomato leucine-rich repeat receptor-like protein LeEix2. *Plant J.* **68**, 413-423. doi:10.1111/j.1365-313X.2011.04696.x
- Smith, S. M., Baker, M., Halebian, M. and Smith, C. J.** (2017). Weak molecular interactions in clathrin-mediated endocytosis. *Front. Mol. Biosci.* **4**, 72. doi:10.3389/fmolb.2017.00072
- Sochacki, K. A. and Taraska, J. W.** (2019). From flat to curved clathrin: controlling a plastic ratchet. *Trends Cell Biol.* **29**, 241-256. doi:10.1016/j.tcb.2018.12.002
- Stefano, G., Renna, L., Wormsbaecher, C., Gamble, J., Zienkiewicz, K. and Brandizzi, F.** (2018). Plant endocytosis requires the ER membrane-anchored proteins VAP27-1 and VAP27-3. *Cell Rep.* **23**, 2299-2307. doi:10.1016/j.celrep.2018.04.091
- Svitkina, T.** (2007). Electron microscopic analysis of the leading edge in migrating cells. *Methods Cell Biol.* **79**, 295-319. doi:10.1016/S0091-679X(06)79012-4
- Takano, J., Miwa, K., Yuan, L., VON Wiren, N. and Fujiwara, T.** (2005). Endocytosis and degradation of BOR1, a boron transporter of Arabidopsis thaliana, regulated by boron availability. *Proc. Natl. Acad. Sci. USA* **102**, 12276-12281. doi:10.1073/pnas.0502060102

- Taylor, M. J., Perrais, D. and Merrifield, C. J.** (2011). A high precision survey of the molecular dynamics of mammalian clathrin-mediated endocytosis. *PLoS Biol.* **9**, e1000604. doi:10.1371/journal.pbio.1000604
- Tinevez, J. Y., Perry, N., Schindelin, J., Hoopes, G. M., Reynolds, G. D., Laplantine, E., Bednarek, S. Y., Shorte, S. L. and Eliceiri, K. W.** (2017). TrackMate: an open and extensible platform for single-particle tracking. *Methods* **115**, 80-90. doi:10.1016/j.ymeth.2016.09.016
- Tokunaga, M., Imamoto, N. and Sakata-Sogawa, K.** (2008). Highly inclined thin illumination enables clear single-molecule imaging in cells. *Nat. Methods* **5**, 159-161. doi:10.1038/nmeth1171
- Vizcay-Barrena, G., Webb, S. E. D., Martin-Fernandez, M. L. and Wilson, Z. A.** (2011). Subcellular and single-molecule imaging of plant fluorescent proteins using total internal reflection fluorescence microscopy (TIRFM). *J. Exp. Bot.* **62**, 5419-5428. doi:10.1093/jxb/err212
- von Kleist, L. and Haucke, V.** (2012). At the crossroads of chemistry and cell biology: inhibiting membrane traffic by small molecules. *Traffic* **13**, 495-504. doi:10.1111/j.1600-0854.2011.01292.x
- Wan, Y., Ash, W. M., III, Fan, L., Hao, H., Kim, M. K. and Lin, J.** (2011). Variable-angle total internal reflection fluorescence microscopy of intact cells of *Arabidopsis thaliana*. *Plant Methods* **7**, 27. doi:10.1186/1746-4811-7-27
- Wang, X., Li, X., Deng, X., Luu, D.-T., Maurel, C. and Lin, J.** (2015). Single-molecule fluorescence imaging to quantify membrane protein dynamics and oligomerization in living plant cells. *Nat. Protoc.* **10**, 2054-2063. doi:10.1038/nprot.2015.132
- Wang, C., Hu, T., Yan, X., Meng, T., Wang, Y., Wang, Q., Zhang, X., Gu, Y., Sánchez-Rodríguez, C., Gadeyne, A. et al.** (2016). Differential regulation of clathrin and its adaptor proteins during membrane recruitment for endocytosis. *Plant Physiol.* **171**, 215-229. doi:10.1104/pp.15.01716
- Wang, J., Mylly, E., Johnson, A., Besbrugge, N., de Jaeger, G., Friml, J., Pleskot, R. and van Damme, D.** (2020). High temporal resolution reveals simultaneous plasma membrane recruitment of the TPLATE complex subunits. *Plant Physiol.* **183**, 986-997. doi:10.1104/pp.20.00178
- Yamaoka, S., Shimono, Y., Shirakawa, M., Fukao, Y., Kawase, T., Hatsugai, N., Tamura, K., Shimada, T. and Hara-Nishimura, I.** (2013). Identification and dynamics of Arabidopsis adaptor protein-2 complex and its involvement in floral organ development. *Plant Cell* **25**, 2958-2969. doi:10.1105/tpc.113.114082
- Yoshinari, A., Fujimoto, M., Ueda, T., Inada, N., Naito, S. and Takano, J.** (2016). DRP1-dependent endocytosis is essential for polar localization and boron-induced degradation of the borate transporter BOR1 in *Arabidopsis thaliana*. *Plant Cell Physiol.* **57**, 1985-2000. doi:10.1093/pcpl/pcw121
- Zhou, J., Liu, D., Wang, P., Ma, X., Lin, W., Chen, S., Mishev, K., Lu, D., Kumar, R., Vanhoutte, I. et al.** (2018). Regulation of Arabidopsis brassinosteroid receptor BRI1 endocytosis and degradation by plant U-box PUB12/PUB13-mediated ubiquitination. *Proc. Natl. Acad. Sci. USA* **115**, E1906-E1915. doi:10.1073/pnas.1712251115
- Zwiewka, M., Nodzyński, T., Robert, S., Vanneste, S. and Friml, J.** (2015). Osmotic stress modulates the balance between exocytosis and clathrin-mediated endocytosis in *Arabidopsis thaliana*. *Mol. Plant* **8**, 1175-1187. doi:10.1016/j.molp.2015.03.007

Supplemental Figures

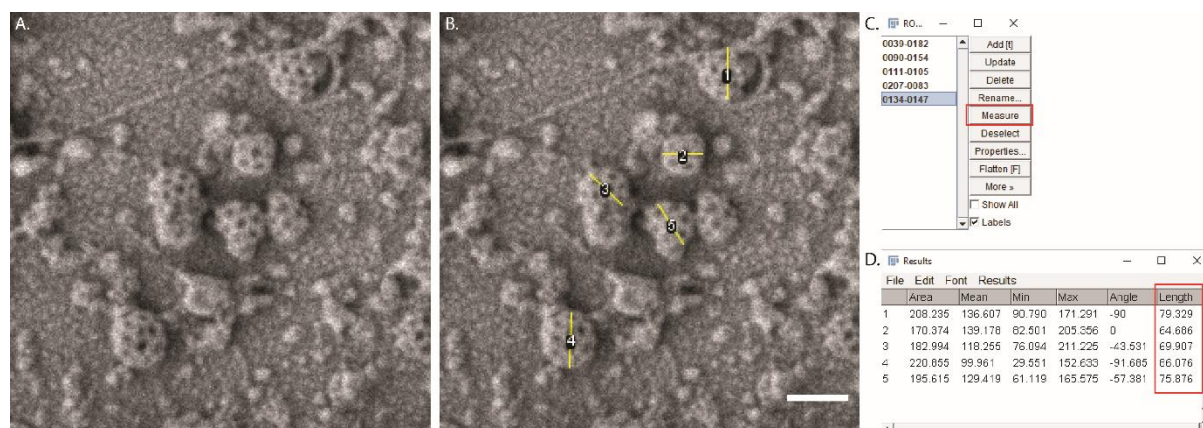


Figure S1 – Measuring the size of CCVs in replica SEM images. (Related to Figure 2).

A) Example CCSs captured by SEM of *Arabidopsis* protoplast metal replicas. B) Line ROIs draw over the diameter of each clearly identify CCS (yellow lines). Scale bar = 100 nm. C) Fiji ROI manager, the red rectangle highlights the measure button used to determine the length of all the ROIs. D) The results of the ROI measurements, the red rectangle highlights the length column of the ROIs.

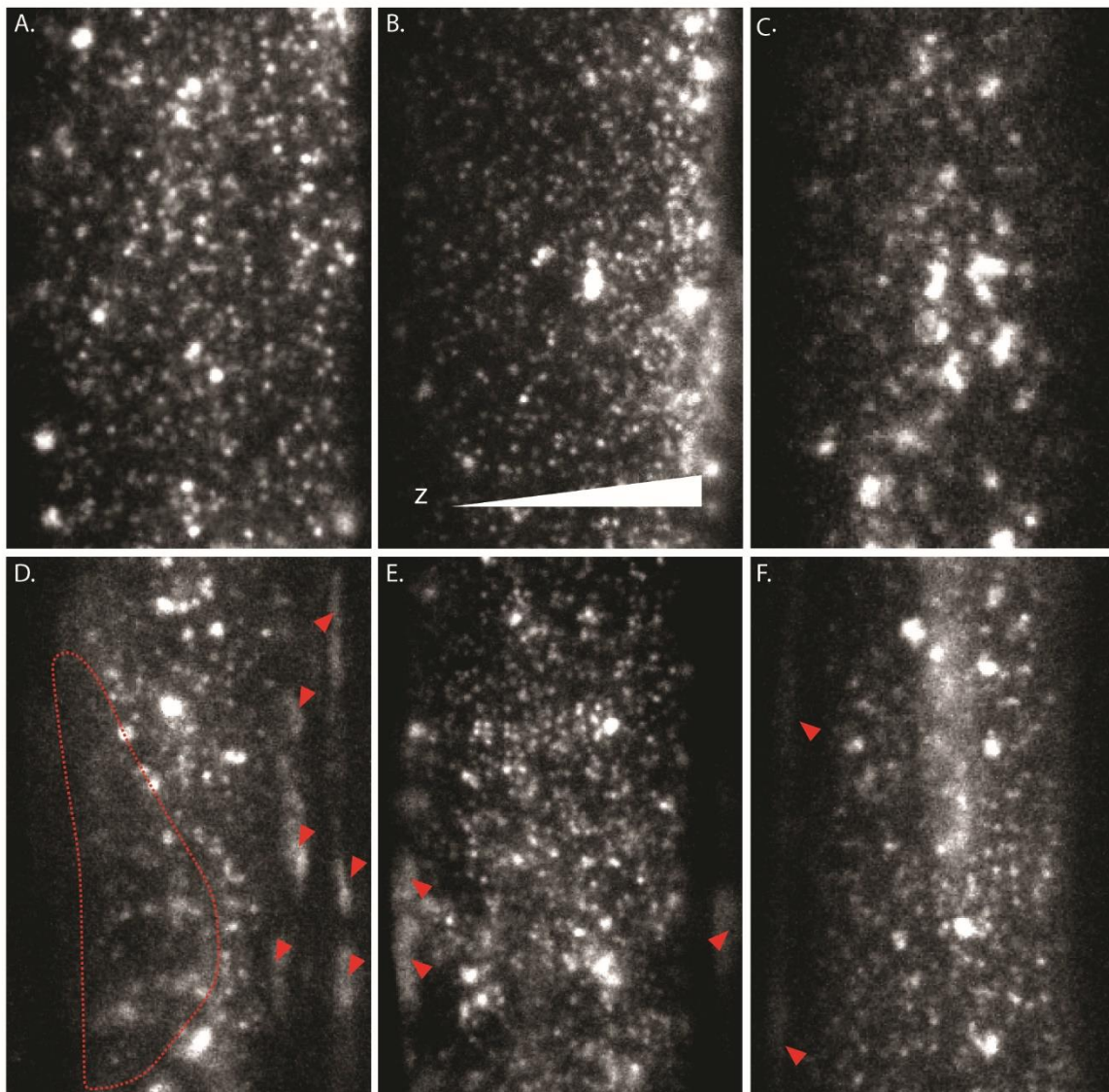


Figure S2 – Comparison of quality of TIRF-M images. (Related to Figures 3, 4 and 5).

Representative TIRF-M image of the epidermal root cells expressing CLC2-GFP. A) shows a good example where the image has a uniform field of illumination across the whole image, and there is an absence of static auto fluorescent signals. Poor examples of TIRF-M images; B) shows image where the TIRF angle is not correctly set, and HILO/VAEM is being used. It is evident based on the non-uniformity of penetration depth of the illumination (white triangle indicates the increase in z penetration), C) shows an out of focus image, D) shows a cell without a flat contact on the coverslip (red dashed line depicts out of contact areas), additionally red arrows note static autofluorescence signals in the field of view, E) shows an image with static autofluorescence signals in the field of view (red arrows), F) shows an image where there is interference of the TIRF-M illumination producing a uniform image of the PM (red-dashed line) and F). Scale bar = 5 μm .

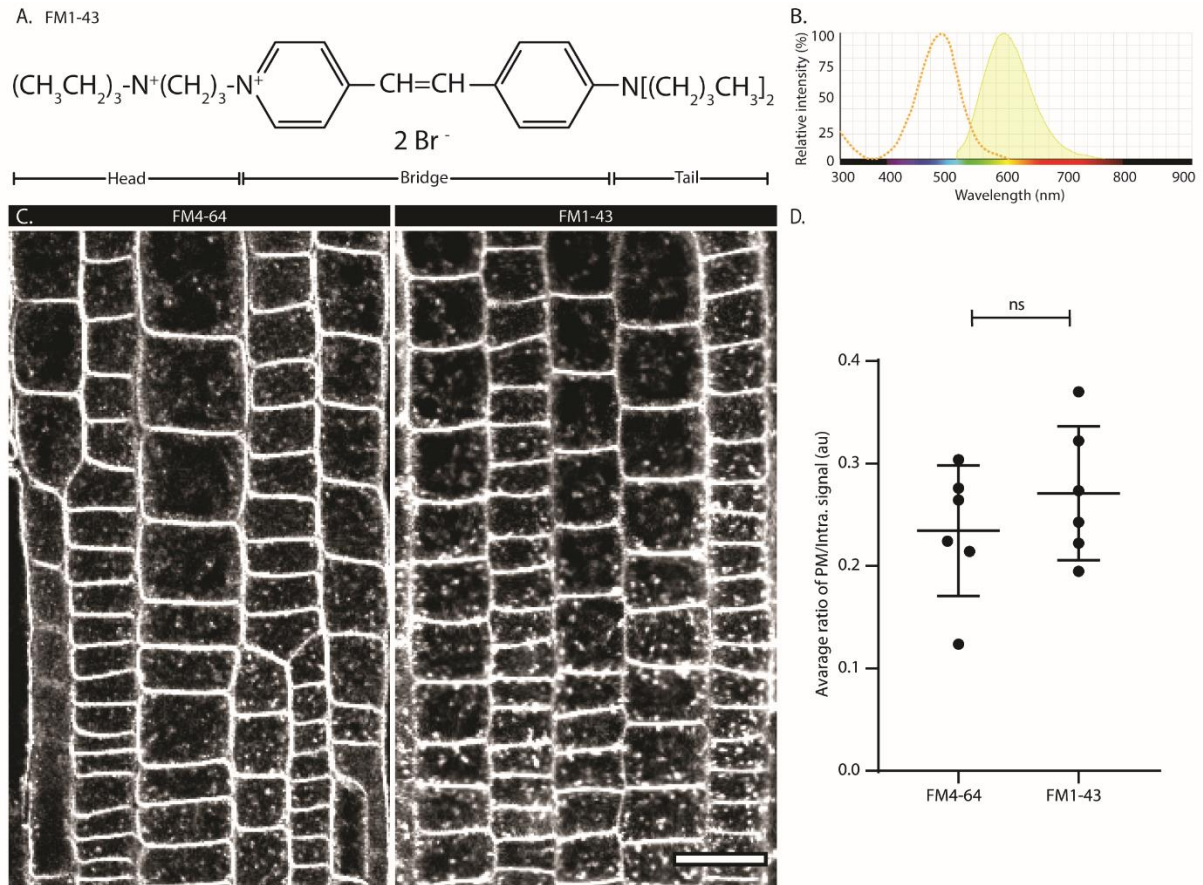


Figure S3 – Comparison of the membrane internalization using FM4-64 and FM1-43.
(Related to Figure 6).

A) Chemical structure of FM1-43. B) The fluorescent spectra of FM1-43 (adapted from ThermoFisher bioscience Fluorescence SpectraViewer). C) Representative confocal images of epidermal root cells incubated with FM4-64 and FM1-43. Scale bar = 20 μm . D) Quantification of FM uptake as determined by the ratio of PM and intra-cellular signal. Plots are mean \pm SEM. N, FM4-64 = 6 individual seedlings, 231 cells; FM1-43 = 6 individual seedlings, 139 cells. T-test, p -value = 0.3501.

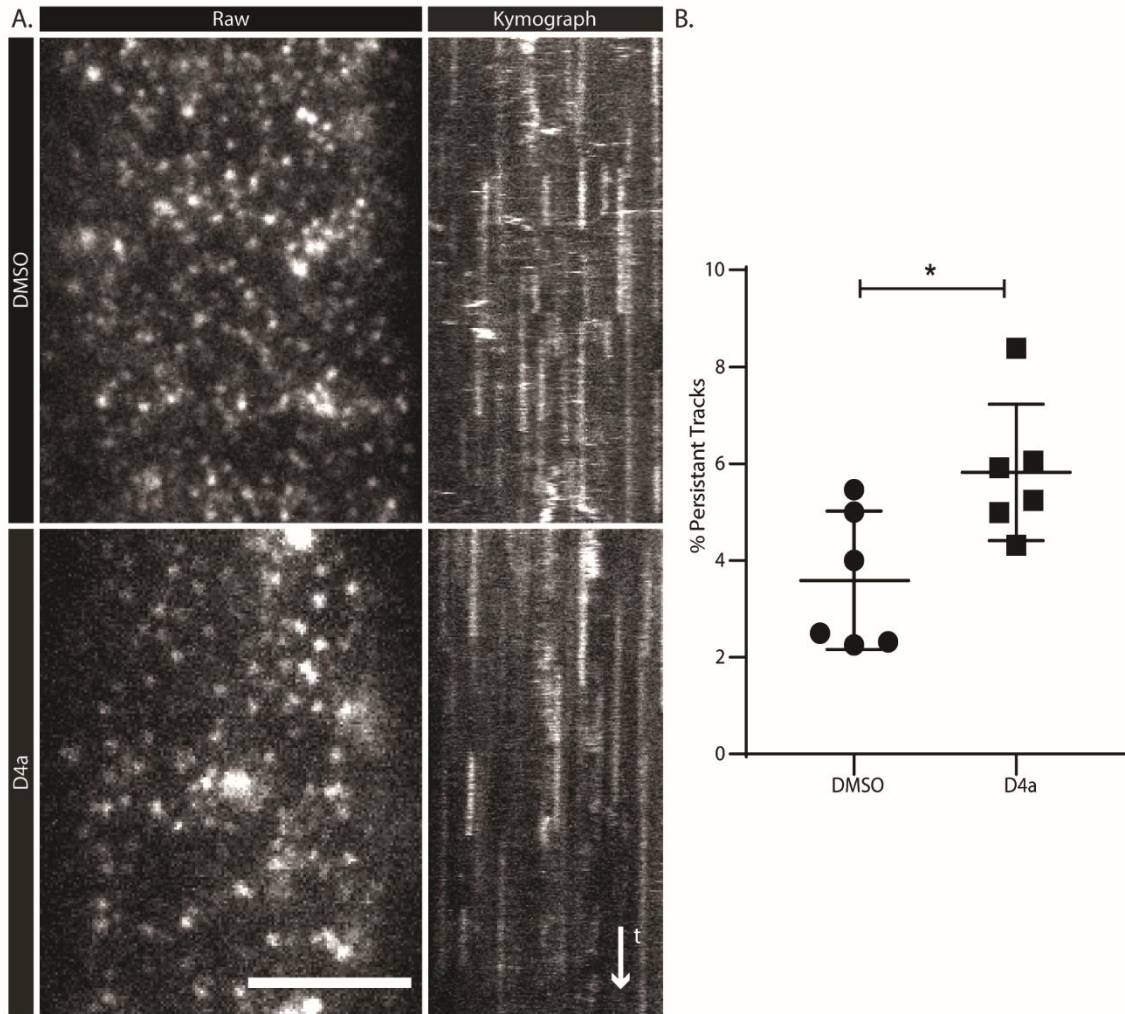


Figure S4 – Effect of Dyngo 4a on CLC-GFP Dynamics.

A) Example of TIRF-M images from the root epidermal cells expressing CLC2-GFP; comparison of mock (DMSO) (upper row) and treatment (Dyngo 4a (D4a), 30 μ M, 15 min) (lower row). Representative kymographs show the effect of treatment on the PM dynamics of CLC2-GFP. Scale bar = 5 μ m. B) Quantification results from combined data of persistent tracks. Plots are mean \pm SEM. N, DMSO = 6 cells from independent roots, 4491 tracks; Dyngo 4a = 6 cells from independent roots, 4700 tracks. T-test, p-value = 0.0217.

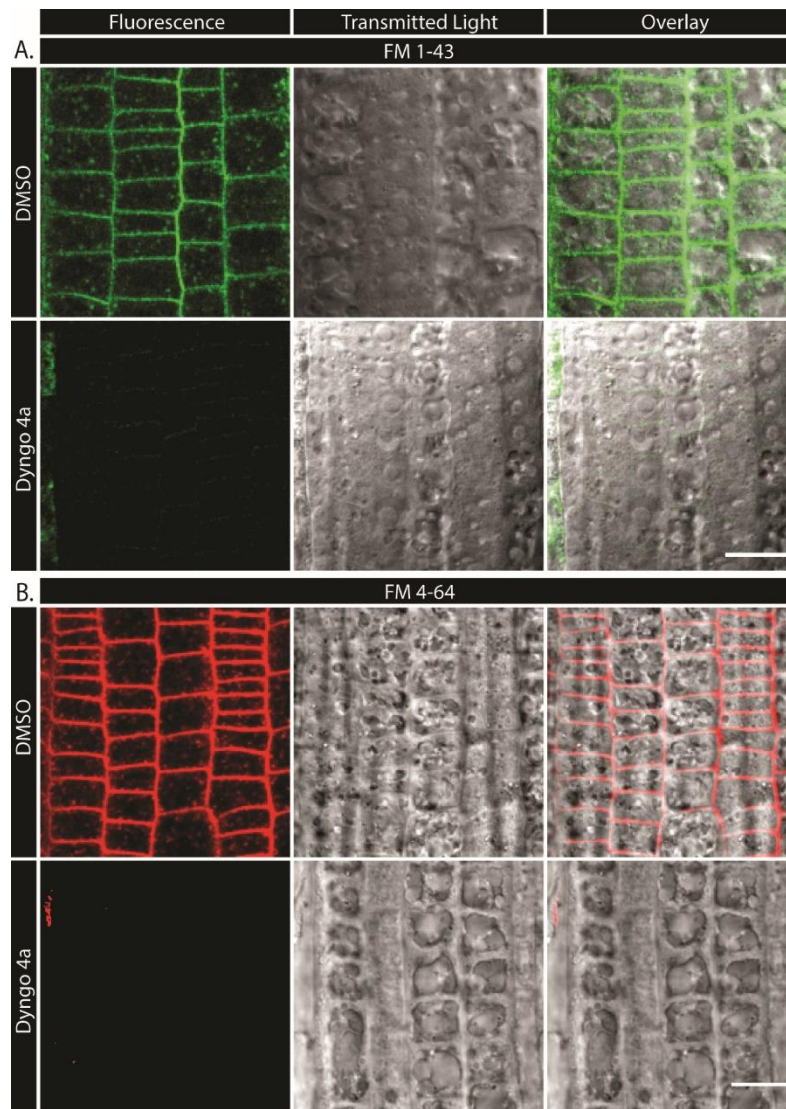


Figure S5 –Dyngo 4a absorbs FM1-43 and FM 4-64 emission. (Related to Figure 6).

Representative confocal images of the epidermal root cells, using the same microscope settings, incubated in control (DMSO) or Dyngo 4a (15 mins 30 μM) conditions in the presence of A) FM1-43 or B) FM4-64 membrane dyes. Scale bars = 20 μm.

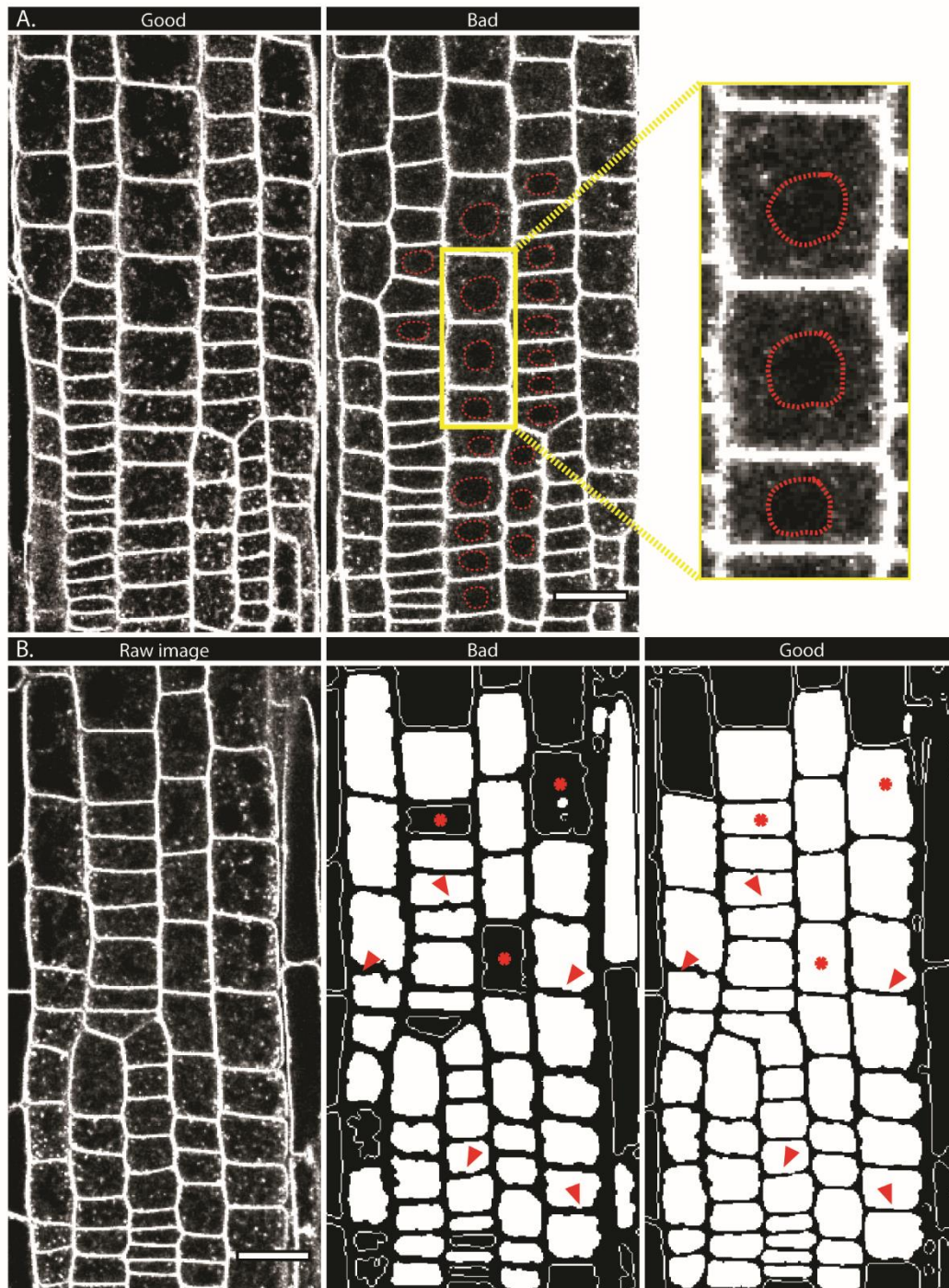


Figure S6 – Comparison of FM cell selection and segmentation. (Related to Figure 6).

A) Examples of poor z plane selection of FM images for analysis. A good example is shown on the left. The bad example (right) has dark black holes in the middles of the cell (red-dashed line outlines the vacuole, image in the middle). The yellow rectangle notes the zoomed in region of the example. B) Representative confocal image of the epidermal root cells incubated with FM4-64 and segmented images with a different threshold. If the threshold for the segmentation of the raw image (on the left) is set incorrectly, the edges of the cells have a lot of prominences (red arrows, middle image). The correct threshold will approximate the outlines to the actual shape of the cells (red arrows, right image). It is important to select only cells which are completely separated and do not interact with the outlines of neighboring cells. Scale bars = 20 μm .

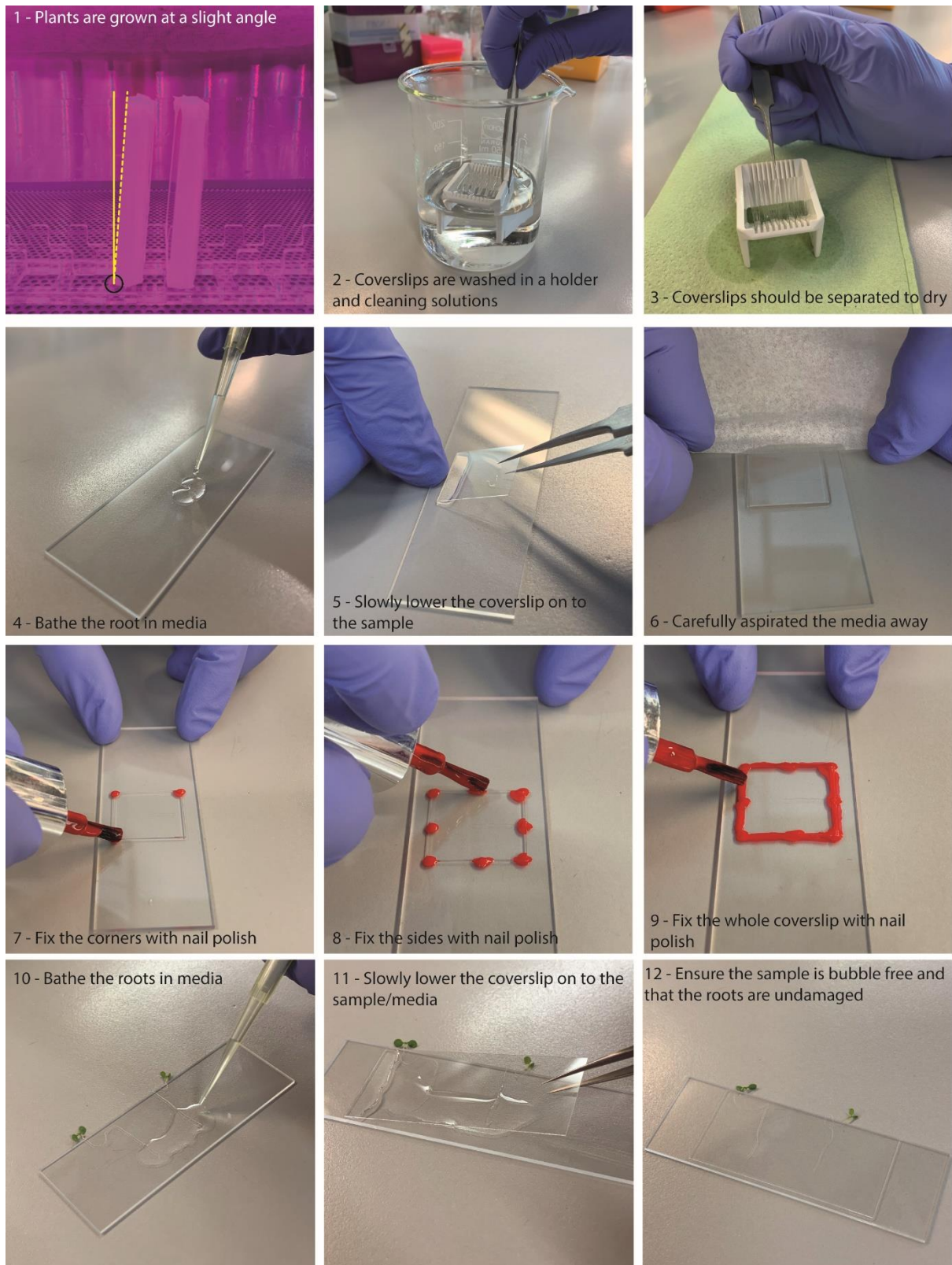


Figure S7

(1-9) Photos of TIRF-M sample preparation. (10-12) photos of FM sample preparation

Supplemental Tables

| | EM | | TIRF-M | Confocal | |
|--|--------------------------|----------------------|--|---------------------------|----------------------|
| | Resin Sections | Metal Replica | | Spinning Disk | CLSM |
| Effective resolution nm (x,y,z) | 4, 4, 40-70 | 4,4,0* | 200, 200, 100 | 200, 200, ~500 | 200, 200, 500 |
| Speed | Fixed | Fixed | Fastest | Fast | Slow |
| Florescence Sensitivity | - | - | High | Low | Low |
| CME Sample prep ease | Extreme | Hard | Hard | Easy | Easy |
| Best Application | Ultrastructural analysis | | Cell surface imaging | | Global uptake assays |
| Major Pro | Resolution | | High signal to noise ratio on cell surface | Can image any tissue type | |
| Major Con | Fixed | | Only cell surface | Low sensitivity for EAPs | |

* There is not effective z resolution, as the image is of the surface of the replica.

Table S1 – Comparison of the selected plant CME imaging technologies

| Protein | Tag | AGI number | Full Construct | Background/ Ecotype | Functionality | References |
|----------------|------------|-------------------|-----------------------|----------------------------|--|--|
| AP2A1 | GFP | AT5G22770 | p35s::AP2A1-GFP | Col-0 | - | (Di Rubbo et al., 2013) |
| AP2A1 | YFP | AT5G22770 | p35s::AP2A1-YFP | Col-0 | - | (Kim et al., 2013) |
| AP2A1 | tagRFP | AT5G22770 | pRPS5A::AP2A1-mTagRFP | Col-0 | - | (Di Rubbo et al., 2013) |
| AP2M | GFP | At4g46630 | pAP2M-AP2M-GFP | <i>ap2m</i> | Complements the significant FM4-64 internalization defect of <i>ap2m</i> | (Yamaoka et al., 2013) |
| AP2M | YFP | At4g46630 | pAP2M-AP2M-GFP | <i>m2-1/Col-0</i> | Complements the significant FM4-64 internalization defect of <i>m2-1</i> | (Bashline et al., 2013) |
| AP2S | GFP | At1g47830 | pAP2S::AP2s-GFP | <i>ap2s</i> | Full rescue of the developmental defects of <i>ap2s</i> | (Fan et al., 2013) |
| AP2S | mCherry | At1g47830 | pAP2S::AP2s-mCherry | Col-0 | - | (Fan et al., 2013) |
| CHC1 | GFP | AT3G11130 | pRPS5A::CHC1-GFP | Col-0 | - | (Dejonghe et al., 2016, Di Rubbo et al., 2013) |
| CLC1 | GFP | AT2G20760 | pCLC1::CLC1-GFP | Col-0 | - | (Di Rubbo et al., 2013) |
| CLC2 | mOrange | AT2G40060 | pCLC2::CLC2-mOrg | WS and Col-0 | - | WS (Konopka et al., 2008); Col-0 (Dejonghe et al., 2016) |
| CLC2 | GFP | AT2G40060 | pCLC2::CLC2-GFP | WS and Col-0 | - | WS (Konopka et al., 2008); Col-0 (Di Rubbo et al., 2013, |

| | | | | | | |
|--------|---------|-----------|-----------------------|----------------------|---|--|
| | | | | | | Fan et al., 2013, Dejonghe et al., 2016) |
| CLC2 | GFP | AT2G40060 | pRPS5A::CHC2-GFP | Col-0 | - | (Ortiz-Morea et al., 2016) |
| CLC2 | mCherry | AT2G40060 | p35s::CLC2-mCherry | Col-0 | - | (Van Damme et al., 2011) |
| CLC2 | tagRFP | AT2G40060 | RPS5Ap::CLC2-TagRFP | Col-0 | - | (Gadeyne et al., 2014) |
| CLC3 | GFP | AT3G51890 | pCLC3::CLC3-GFP | Col-0 | - | (Di Rubbo et al., 2013) |
| Drp1a | mOrange | AT5G42080 | pDrp1a::Drp1a-mOrange | <i>drp1a-2</i> /WS | Complements the infertility of <i>drp1a</i> mutant | (Konopka and Bednarek, 2008) |
| Drp1a | RFP | AT5G42080 | p35s::Drp1a-mRFP1 | <i>drp1a</i> /Col-0 | Rescue of the developmental phenotypes of <i>drp1a</i> mutant plants | (Fujimoto et al., 2008, Mravec et al., 2011) |
| Drp1c | GFP | AT1G14830 | pDrp1c::Drp1c-GFP | <i>drp1c-1</i> /WS | Rescue of the development of <i>drp1C-1</i> pollen | (Konopka et al., 2008) |
| Drp2a | GFP | AT1G10290 | pDrp2a::Drp2a-GFP | Col-0 | - | (Huang et al., 2015) |
| Drp2b | tagRFP | AT1G59610 | pDrp2b::Drp2b-tagRFP | Col-0 | - | (Huang et al., 2015) |
| Drp2b | GFP | AT1G59610 | p35s::Drp2b-GFP | Col-0 | - | (Fujimoto et al., 2008) |
| TPLATE | GFP | AT3G01780 | pTPLATE::TPLATE-GFP | <i>tplate</i> /Col-0 | Rescue of the homozygous <i>tplate</i> mutant | (Gadeyne et al., 2014) |
| TML | GFP | AT5G57460 | pTML::TML-GFP | <i>tml-1</i> /Col-0 | Rescue of the male transmission failure of both <i>tml-1</i> / <i>tml-2</i> mutant allele | (Gadeyne et al., 2014) |

| | | | | | | |
|---------|-----|-----------|-----------------------|------------------------|--|-------------------------|
| TML | YFP | AT5G57460 | pTML::TML-YFP | <i>tml-1/Col-0</i> | Rescue of the male transmission failure of both <i>tml-1/tml-2</i> mutant allele | (Gadeyne et al., 2014) |
| LOLITA | GFP | AT1G15370 | p35s::LOLITA-GFP | Col-0 | - | (Gadeyne et al., 2014) |
| TWD40-2 | GFP | AT5G24710 | p35s::TWD40-2-GFP | Col-0 | - | (Gadeyne et al., 2014) |
| TWD40-2 | GFP | AT5G24710 | pTWD40-2::GFP-TWD40-2 | <i>twd40-2-3/Col-0</i> | Rescue of the growth defects of <i>twd40-2-3</i> | (Bashline et al., 2015) |
| TASH3 | GFP | AT2G07360 | p35s::TASH3-GFP | Col-0 | - | (Gadeyne et al., 2014) |
| atEH1 | GFP | AT1G20760 | p35s::atEH1-GFP | Col-0 | - | (Gadeyne et al., 2014) |
| atEH2 | GFP | AT1G21630 | p35s::atEH2-GFP | Col-0 | - | (Gadeyne et al., 2014) |

Table S2 – Examples of key published Fluorescent clathrin and EAP markers lines

Table S2 – Published Fluorescent clathrin and EAP markers lines

| Drug | Effect | Mechanism | Notes | Plant Tissue Tested | Ref |
|-------------|---|--------------------------------|---|---|--|
| Dynasore | Inhibited cargo internalization | Dynamin GTPase inhibitor | Reported off tagged effects on membrane ruffling | <i>Nicotiana benthamiana</i> | (Sharfman et al., 2011) |
| Dyngo 4a | Prolonged CLC2 lifetime, reduced fixable FM uptake, block cargo uptake | Dynamin GTPase inhibitor | Absorbs light 500-700 nm, therefore not suitable for red imaging | Seedlings, <i>Nicotiana benthamiana</i> | (Hunter et al., 2019, Zhang et al., 2017) and Figure S5 |
| ES9 | Very strong block of FM uptake, prolonged cell surface lifetime of EAPs | Binds CHC | It is a protonophore | Seedlings | (Dejonghe et al., 2016) |
| ES9-17 | Very strong block of FM uptake, prolonged cell surface lifetime of EAPs | Binds CHC | Targets CHC, which is involved in other clathrin mediated processes | Seedlings | (Dejonghe et al., 2019) |
| IKA | Reduced FM uptake, prolonged cell surface lifetime of EAPs | Unknown | Appears to be specific for CME, however caution should be used as its mechanistic function is unknown | Seedlings, Pollen Tube, BY2 cells | (Bandmann et al., 2012, Elkin et al., 2016, Moscatelli et al., 2007) and Figures 7 and 8 |
| Pitstop-2 | Reduced FM uptake | Disrupts clathrin interactions | Not CME specific and did not effect block internalization of cargo | Seedlings | (Dejonghe et al., 2019, Dutta et al., 2012, von Kleist et al., 2011) |

Table S3 – Chemical inhibitors of plant CME

| Protein | Gene | AGI number | Function in CME | Modification | Phenotype | Tissue | References |
|----------|--------------|------------|--|--------------------------------------|--|--|---|
| Clathrin | <i>CHC1</i> | AT3G11130 | Formation of clathrin triskelion | pINTAM>>RFP-HUB1 | Endocytic defect (inhibition of FM4-64 internalization) | Root, BY-2 cells | (Dhonukshe et al., 2007), (Tahara et al., 2007), (Robert et al., 2010), (Kitakura et al., 2011) |
| AP-2 | <i>AP2A1</i> | AT5G22770 | Adaptor complex that interacts with the membrane, clathrin, and CME accessory proteins and cargo | AP2A-RNAi | Endocytic defect (inhibition of FM4-64 internalization in root epidermal cells) | Root | (Di Rubbo et al., 2013) |
| | <i>AP2A2</i> | AT5G22780 | | | | | |
| | <i>AP2M</i> | AT5G46630 | | AP2MΔC | Endocytic defect (inhibition of FM4-64 internalization in root epidermal cells, defect in formation of BFA bodies) | Root | (Di Rubbo et al., 2013), (Owen and Evans, 1998) |
| AP180 | <i>AP180</i> | AT1G05020 | Adaptor protein involved in clathrin-mediated endocytosis | At-AP180ΔENTH truncated version | No showed effect <i>in vitro</i> | Cell suspension cultures of <i>A. thaliana</i> | (Barth and Holstein, 2004) |
| Dynamins | <i>DRPIA</i> | AT5G42080 | CCV scission from PM / Putative role in CCV scission | K47A point mutation in GTPase domain | Longer CLC lifetime | Root | (Yoshinari et al., 2016) |
| | <i>DRP2A</i> | AT1G10290 | | Inducible Strep-DRP2A-K51E | Endocytic defect (reduced endocytosis in root hairs; bulging of the tip of root hairs, | Root | (Taylor et al., 2011) |
| | <i>DRP2B</i> | AT1G59610 | | Inducible Strep-DRP2B-K51E | | | |

| | | | | | | | |
|----------------|----------------------|-----------|---|--|---|------|--|
| | | | | | and bursting of root hairs at the very tip) Mutant cannot complement the knock-out phenotype | | |
| | <i>DRPIE</i> | AT3G60190 | Potentially involved in CCV scission from PM | P77L point mutation in GTPase domain | gain-of-function phenotype | Root | (Tang et al., 2006) |
| Auxilin | <i>AUXILIN-LIKE1</i> | AT4G12780 | Negative regulation of endocytosis | XVE» <i>AUXILIN-LIKE1/2</i> | Block of endocytosis after the initial step by inhibition of recruitment of clathrin | Root | (Adamowski et al., 2018, Ortiz-Morea et al., 2016) |
| TPLATE complex | <i>TML</i> | AT5G57460 | TPLATE complex subunit involved in clathrin mediated endocytosis. | Truncated TML <i>TMLΔC</i> <i>amiR-TML</i> | Endocytic defect (inhibition of FM4-64 internalization, defect in formation of BFA bodies, reduction in TPC complex size) | Root | (Gadeyne et al., 2014) |
| | <i>TPLATE</i> | AT3G01780 | | <i>amiR-TPLATE</i> | | | |

Table S4 – Published genetic manipulations of plant CME

| | FM | Photoconvertible fluorophore (e.g., Dendra) | BFA |
|----------------------|--|---|------------------------------------|
| Tissue tested | Protoplasts and plants | Plants | Protoplasts and plants |
| Ease | Application/incubation of dye | Requires cloning and transformation | Application/incubation of compound |
| Specificity | Not specific for CME, but total PM internalization | Dependent on cargo studied | Dependent on cargo studied |
| Pros | Rapid and direct measure of PM endocytosis | Specific for a certain cargo | Rapid to establish assay |
| Cons | Not specific for CME | Takes time to generate material and cargo pathway must be known | Artificial BFA body |

Table S5 – Summary of example global uptake methods

| Protein | Gene | AGI number | Phenotype | References |
|----------------|----------------------|-------------------|---|--|
| Clathrin | <i>chc1</i> | AT3G11130 | Reduced rates of endocytosis and defects clathrin mediated exocytosis | (Alonso et al., 2003), (Kitakura et al., 2011), (Larson et al., 2017) |
| | <i>chc2</i> | AT3G08530 | Reduced rates of endocytosis and defects clathrin mediated exocytosis | |
| | <i>clc1</i> | AT2G40060 | In homozygous form pollen is not viable | (Alonso et al., 2003), (Wang et al., 2013) |
| | <i>clc2</i> | AT2G20760 | Numerous developmental defects | |
| | <i>clc3</i> | AT3G51890 | Numerous developmental defects | |
| AP-2 | <i>ap2m</i> | AT5G46630 | Showed many developmental defects, including abnormal phyllotaxis, an increase in the number of shoots and branches, smaller leaves, an increase in the leaf number, and shorter root hairs | (Alonso et al., 2003), (Bashline et al., 2013, Kim et al., 2013, Yamaoka et al., 2013) |
| | <i>ap2s</i> | AT1G47830 | Localization and dynamics of CLC-EGFP are altered | (Alonso et al., 2003), (Fan et al., 2013) |
| AP180 | <i>ap180</i> | AT2G25430 | No obvious growth or developmental defects were observed | (Alonso et al., 2003), (Kaneda et al., 2019) |
| Dynamins | <i>drp1a</i> | AT5G42080 | Inhibits fertilization due to maternal sporophytic defect | (Alonso et al., 2003), (Kang et al., 2003a) |
| | <i>drp1c</i> | AT1G14830 | Homozygous lethal (disrupts post-meiotic pollen development) | (Kang et al., 2003b) |
| | <i>drp1e</i> | AT3G60190 | Null mutants have defects of cell plate formation in root and arrest of embryo development; enhanced cell death in response to powdery mildew infection | (Alonso et al., 2003), (Fujimoto and Tsutsumi, 2014, Tang et al., 2006), |
| | <i>drp2a</i> | AT1G10290 | No obvious growth or developmental defects were observed | (Alonso et al., 2003), (Backues et al., 2010) |
| | <i>drp2b</i> | AT1G59610 | No obvious growth or developmental defects were observed | |
| Auxilin | <i>auxilin-like1</i> | AT4G12780 | Phenotypically normal | (Adamowski et al., 2018) |
| | <i>auxilin-like2</i> | AT4G12770 | Phenotypically normal | |
| TPLATE complex | <i>tplate</i> | AT1G07670 | Embryo-lethal | (Alonso et al., 2003), (Gadeyne et al., 2014) |
| | <i>tml</i> | AT5G57460 | Embryo-lethal | |

| | | | | |
|--|----------------|-----------|--------------------------------------|---|
| | <i>twd40-2</i> | AT5G24710 | Reduced rates of membrane dye uptake | (Alonso et al., 2003), (Bashline et al., 2015) |
|--|----------------|-----------|--------------------------------------|---|

Table S6 – Published and characterized mutant EAP lines

Supplemental References

- ADAMOWSKI, M., NARASIMHAN, M., KANIA, U., GLANC, M., DE JAEGER, G. & FRIML, J. 2018. A Functional Study of AUXILIN-LIKE1 and 2, Two Putative Clathrin Uncoating Factors in Arabidopsis. *Plant Cell*, 30, 700-716.
- ALONSO, J. M., STEPANOVA, A. N., LEISSE, T. J., KIM, C. J., CHEN, H., SHINN, P., STEVENSON, D. K., ZIMMERMAN, J., BARAJAS, P., CHEUK, R., GADRINAB, C., HELLER, C., JESKE, A., KOESEMA, E., MEYERS, C. C., PARKER, H., PREDNIS, L., ANSARI, Y., CHOY, N., DEEN, H., GERALT, M., HAZARI, N., HOM, E., KARNES, M., MULHOLLAND, C., NDUBAKU, R., SCHMIDT, I., GUZMAN, P., AGUILAR-HENONIN, L., SCHMID, M., WEIGEL, D., CARTER, D. E., MARCHAND, T., RISSEEUW, E., BROGDEN, D., ZEKO, A., CROSBY, W. L., BERRY, C. C. & ECKER, J. R. 2003. Genome-wide insertional mutagenesis of Arabidopsis thaliana. *Science*, 301, 653-7.
- BACKUES, S. K., KORASICK, D. A., HEESE, A. & BEDNAREK, S. Y. 2010. The Arabidopsis dynamin-related protein2 family is essential for gametophyte development. *Plant Cell*, 22, 3218-31.
- BANDMANN, V., MULLER, J. D., KOHLER, T. & HOMANN, U. 2012. Uptake of fluorescent nano beads into BY2-cells involves clathrin-dependent and clathrin-independent endocytosis. *FEBS Lett*, 586, 3626-32.
- BARTH, M. & HOLSTEIN, S. E. 2004. Identification and functional characterization of Arabidopsis AP180, a binding partner of plant alphaC-adaptin. *J Cell Sci*, 117, 2051-62.
- BASHLINE, L., LI, S., ANDERSON, C. T., LEI, L. & GU, Y. 2013. The endocytosis of cellulose synthase in Arabidopsis is dependent on mu2, a clathrin-mediated endocytosis adaptin. *Plant Physiol*, 163, 150-60.
- BASHLINE, L., LI, S., ZHU, X. & GU, Y. 2015. The TWD40-2 protein and the AP2 complex cooperate in the clathrin-mediated endocytosis of cellulose synthase to regulate cellulose biosynthesis. *Proc Natl Acad Sci U S A*, 112, 12870-5.
- DEJONGHE, W., KUENEN, S., MYLLE, E., VASILEVA, M., KEECH, O., VIOTTI, C., SWERTS, J., FENDRYCH, M., ORTIZ-MOREA, F. A., MISHEV, K., DELANG, S., SCHOLL, S., ZARZA, X., HEILMANN, M., KOURELIS, J., KASPROWICZ, J., NGUYEN LE, S. L., DROZDZECKI, A., VAN HOUTTE, I., SZATMARI, A. M., MAJDA, M., BAISA, G., BEDNAREK, S. Y., ROBERT, S., AUDENAERT, D., TESTERINK, C., MUNNIK, T., VAN DAMME, D., HEILMANN, I., SCHUMACHER, K., WINNE, J., FRIML, J., VERSTREKEN, P. & RUSSINOVA, E. 2016. Mitochondrial uncouplers inhibit clathrin-mediated endocytosis largely through cytoplasmic acidification. *Nat Commun*, 7, 11710.
- DEJONGHE, W., SHARMA, I., DENOO, B., DE MUNCK, S., LU, Q., MISHEV, K., BULUT, H., MYLLE, E., DE RYCKE, R., VASILEVA, M., SAVATIN, D. V., NERINCKX, W., STAES, A., DROZDZECKI, A., AUDENAERT, D., YPERMAN, K., MADDER, A., FRIML, J., VAN DAMME, D., GEVAERT, K., HAUCKE, V., SAVVIDES, S. N., WINNE, J. & RUSSINOVA, E. 2019. Disruption of endocytosis through chemical inhibition of clathrin heavy chain function. *Nat Chem Biol*, 15, 641-649.
- DHONUKSHE, P., ANIENTO, F., HWANG, I., ROBINSON, D. G., MRAVEC, J., STIERHOF, Y. D. & FRIML, J. 2007. Clathrin-mediated constitutive endocytosis of PIN auxin efflux carriers in Arabidopsis. *Curr Biol*, 17, 520-7.
- DI RUBBO, S., IRANI, N. G., KIM, S. Y., XU, Z. Y., GADEYNE, A., DEJONGHE, W., VANHOUTTE, I., PERSIAU, G., EECKHOUT, D., SIMON, S., SONG, K., KLEINE-

- VEHN, J., FRIML, J., DE JAEGER, G., VAN DAMME, D., HWANG, I. & RUSSINOVA, E. 2013. The clathrin adaptor complex AP-2 mediates endocytosis of brassinosteroid insensitive1 in Arabidopsis. *Plant Cell*, 25, 2986-97.
- DUTTA, D., WILLIAMSON, C. D., COLE, N. B. & DONALDSON, J. G. 2012. Pitstop 2 is a potent inhibitor of clathrin-independent endocytosis. *PLoS One*, 7, e45799.
- ELKIN, S. R., OSWALD, N. W., REED, D. K., METTLEN, M., MACMILLAN, J. B. & SCHMID, S. L. 2016. Ikarugamycin: A Natural Product Inhibitor of Clathrin-Mediated Endocytosis. *Traffic*, 17, 1139-49.
- FAN, L., HAO, H., XUE, Y., ZHANG, L., SONG, K., DING, Z., BOTELLA, M. A., WANG, H. & LIN, J. 2013. Dynamic analysis of Arabidopsis AP2 sigma subunit reveals a key role in clathrin-mediated endocytosis and plant development. *Development*, 140, 3826-37.
- FUJIMOTO, M., ARIMURA, S., NAKAZONO, M. & TSUTSUMI, N. 2008. Arabidopsis dynamin-related protein DRP2B is co-localized with DRP1A on the leading edge of the forming cell plate. *Plant Cell Rep*, 27, 1581-6.
- FUJIMOTO, M. & TSUTSUMI, N. 2014. Dynamin-related proteins in plant post-Golgi traffic. *Front Plant Sci*, 5, 408.
- GADEYNE, A., SANCHEZ-RODRIGUEZ, C., VANNESTE, S., DI RUBBO, S., ZAUBER, H., VANNESTE, K., VAN LEENE, J., DE WINNE, N., EECKHOUT, D., PERSIAU, G., VAN DE SLIJKE, E., CANNOOT, B., VERCRUYSSSE, L., MAYERS, J. R., ADAMOWSKI, M., KANIA, U., EHRLICH, M., SCHWEIGHOFER, A., KETELAAR, T., MAERE, S., BEDNAREK, S. Y., FRIML, J., GEVAERT, K., WITTERS, E., RUSSINOVA, E., PERSSON, S., DE JAEGER, G. & VAN DAMME, D. 2014. The TPLATE adaptor complex drives clathrin-mediated endocytosis in plants. *Cell*, 156, 691-704.
- HUANG, J., FUJIMOTO, M., FUJIWARA, M., FUKAO, Y., ARIMURA, S. & TSUTSUMI, N. 2015. Arabidopsis dynamin-related proteins, DRP2A and DRP2B, function coordinately in post-Golgi trafficking. *Biochem Biophys Res Commun*, 456, 238-44.
- HUNTER, K., KIMURA, S., ROKKA, A., TRAN, H. C., TOYOTA, M., KUKKONEN, J. P. & WRZACZEK, M. 2019. CRK2 Enhances Salt Tolerance by Regulating Callose Deposition in Connection with PLDalpha1. *Plant Physiol*, 180, 2004-2021.
- KANEDA, M., VAN OOSTENDE-TRIPLET, C., CHEBLI, Y., TESTERINK, C., BEDNAREK, S. Y. & GEITMANN, A. 2019. Plant AP180 N-Terminal Homolog Proteins Are Involved in Clathrin-Dependent Endocytosis during Pollen Tube Growth in Arabidopsis thaliana. *Plant Cell Physiol*, 60, 1316-1330.
- KANG, B. H., BUSSE, J. S. & BEDNAREK, S. Y. 2003a. Members of the Arabidopsis dynamin-like gene family, ADL1, are essential for plant cytokinesis and polarized cell growth. *Plant Cell*, 15, 899-913.
- KANG, B. H., RANCOUR, D. M. & BEDNAREK, S. Y. 2003b. The dynamin-like protein ADL1C is essential for plasma membrane maintenance during pollen maturation. *Plant J*, 35, 1-15.
- KIM, S. Y., XU, Z. Y., SONG, K., KIM, D. H., KANG, H., REICHARDT, I., SOHN, E. J., FRIML, J., JUERGENS, G. & HWANG, I. 2013. Adaptor protein complex 2-mediated endocytosis is crucial for male reproductive organ development in Arabidopsis. *Plant Cell*, 25, 2970-85.
- KITAKURA, S., VANNESTE, S., ROBERT, S., LOFKE, C., TEICHMANN, T., TANAKA, H. & FRIML, J. 2011. Clathrin mediates endocytosis and polar distribution of PIN auxin transporters in Arabidopsis. *Plant Cell*, 23, 1920-31.

- KONOPKA, C. A., BACKUES, S. K. & BEDNAREK, S. Y. 2008. Dynamics of Arabidopsis dynamin-related protein 1C and a clathrin light chain at the plasma membrane. *Plant Cell*, 20, 1363-80.
- KONOPKA, C. A. & BEDNAREK, S. Y. 2008. Comparison of the dynamics and functional redundancy of the Arabidopsis dynamin-related isoforms DRP1A and DRP1C during plant development. *Plant Physiol*, 147, 1590-602.
- LARSON, E. R., VAN ZELM, E., ROUX, C., MARION-POLL, A. & BLATT, M. R. 2017. Clathrin Heavy Chain Subunits Coordinate Endo- and Exocytic Traffic and Affect Stomatal Movement. *Plant Physiol*, 175, 708-720.
- MOSCATELLI, A., CIAMPOLINI, F., RODIGHIERO, S., ONELLI, E., CRESTI, M., SANTO, N. & IDILLI, A. 2007. Distinct endocytic pathways identified in tobacco pollen tubes using charged nanogold. *J Cell Sci*, 120, 3804-19.
- MRAVEC, J., PETRASEK, J., LI, N., BOEREN, S., KARLOVA, R., KITAKURA, S., PAREZOVA, M., NARAMOTO, S., NODZYNSKI, T., DHONUKSHE, P., BEDNAREK, S. Y., ZAZIMALOVA, E., DE VRIES, S. & FRIML, J. 2011. Cell plate restricted association of DRP1A and PIN proteins is required for cell polarity establishment in Arabidopsis. *Curr Biol*, 21, 1055-60.
- ORTIZ-MOREA, F. A., SAVATIN, D. V., DEJONGHE, W., KUMAR, R., LUO, Y., ADAMOWSKI, M., VAN DEN BEGIN, J., DRESSANO, K., PEREIRA DE OLIVEIRA, G., ZHAO, X., LU, Q., MADDER, A., FRIML, J., SCHERER DE MOURA, D. & RUSSINOVA, E. 2016. Danger-associated peptide signaling in Arabidopsis requires clathrin. *Proc Natl Acad Sci U S A*, 113, 11028-33.
- OWEN, D. J. & EVANS, P. R. 1998. A structural explanation for the recognition of tyrosine-based endocytotic signals. *Science*, 282, 1327-32.
- ROBERT, S., KLEINE-VEHN, J., BARBEZ, E., SAUER, M., PACIOREK, T., BASTER, P., VANNESTE, S., ZHANG, J., SIMON, S., COVANOVA, M., HAYASHI, K., DHONUKSHE, P., YANG, Z., BEDNAREK, S. Y., JONES, A. M., LUSCHNIG, C., ANIENTO, F., ZAZIMALOVA, E. & FRIML, J. 2010. ABP1 mediates auxin inhibition of clathrin-dependent endocytosis in Arabidopsis. *Cell*, 143, 111-21.
- SHARFMAN, M., BAR, M., EHRLICH, M., SCHUSTER, S., MELECH-BONFIL, S., EZER, R., SESSA, G. & AVNI, A. 2011. Endosomal signaling of the tomato leucine-rich repeat receptor-like protein LeEix2. *Plant J*, 68, 413-23.
- TAHARA, H., YOKOTA, E., IGARASHI, H., ORII, H., YAO, M., SONOBE, S., HASHIMOTO, T., HUSSEY, P. J. & SHIMMEN, T. 2007. Clathrin is involved in organization of mitotic spindle and phragmoplast as well as in endocytosis in tobacco cell cultures. *Protoplasma*, 230, 1-11.
- TANG, D., ADE, J., FRYE, C. A. & INNES, R. W. 2006. A mutation in the GTP hydrolysis site of Arabidopsis dynamin-related protein 1E confers enhanced cell death in response to powdery mildew infection. *Plant J*, 47, 75-84.
- TAYLOR, M. J., PERRAIS, D. & MERRIFIELD, C. J. 2011. A high precision survey of the molecular dynamics of mammalian clathrin-mediated endocytosis. *PLoS Biol*, 9, e1000604.
- VAN DAMME, D., GADEYNE, A., VANSTRAELEN, M., INZE, D., VAN MONTAGU, M. C., DE JAEGER, G., RUSSINOVA, E. & GEELLEN, D. 2011. Adaptin-like protein TPLATE and clathrin recruitment during plant somatic cytokinesis occurs via two distinct pathways. *Proc Natl Acad Sci U S A*, 108, 615-20.
- VON KLEIST, L., STAHLSCHEIDT, W., BULUT, H., GROMOVA, K., PUCHKOV, D., ROBERTSON, M. J., MACGREGOR, K. A., TOMILIN, N., PECHSTEIN, A., CHAU, N., CHIRCOP, M., SAKOFF, J., VON KRIES, J. P., SAENGER, W., KRAUSSLICH, H. G., SHUPLIAKOV, O., ROBINSON, P. J., MCCLUSKEY, A. & HAUCKE, V.

2011. Role of the clathrin terminal domain in regulating coated pit dynamics revealed by small molecule inhibition. *Cell*, 146, 471-84.
- WANG, C., YAN, X., CHEN, Q., JIANG, N., FU, W., MA, B., LIU, J., LI, C., BEDNAREK, S. Y. & PAN, J. 2013. Clathrin light chains regulate clathrin-mediated trafficking, auxin signaling, and development in Arabidopsis. *Plant Cell*, 25, 499-516.
- YAMAOKA, S., SHIMONO, Y., SHIRAKAWA, M., FUKAO, Y., KAWASE, T., HATSUGAI, N., TAMURA, K., SHIMADA, T. & HARA-NISHIMURA, I. 2013. Identification and dynamics of Arabidopsis adaptor protein-2 complex and its involvement in floral organ development. *Plant Cell*, 25, 2958-69.
- YOSHINARI, A., FUJIMOTO, M., UEDA, T., INADA, N., NAITO, S. & TAKANO, J. 2016. DRP1-Dependent Endocytosis is Essential for Polar Localization and Boron-Induced Degradation of the Borate Transporter BOR1 in Arabidopsis thaliana. *Plant Cell Physiol*, 57, 1985-2000.
- ZHANG, H. M., COLYVAS, K., PATRICK, J. W. & OFFLER, C. E. 2017. A Ca²⁺-dependent remodelled actin network directs vesicle trafficking to build wall ingrowth papillae in transfer cells. *J Exp Bot*, 68, 4749-4764.